doi:10.1093/brain/awaa376 BRAIN 2021: 144; 288–309 | 288

BRAIN
A JOURNAL OF NEUROLOGY

Alzheimer's disease brain-derived extracellular vesicles spread tau pathology in interneurons

Zhi Ruan,[1] Dhruba Pathak,[1,2] Srinidhi Venkatesan Kalavai,[1] Asuka Yoshii-Kitahara,[1] Satoshi Muraoka,[1] Nemil Bhatt,[3] Kayo Takamatsu-Yukawa,[1] Jianqiao Hu,[1] Yuzhi Wang,[1] Samuel Hersh,[1] Maria Ericsson,[4] Santhi Gorantla,[5] Howard E. Gendelman,[5] Rakez Kayed,[3] Seiko Ikezu,[1] Jennifer I. Luebke[2,6] and Tsuneya Ikezu[1,6,7]

Extracellular vesicles are highly transmissible and play critical roles in the propagation of tau pathology, although the underlying mechanism remains elusive. Here, for the first time, we comprehensively characterized the physicochemical structure and pathogenic function of human brain-derived extracellular vesicles isolated from Alzheimer's disease, prodromal Alzheimer's disease, and non-demented control cases. Alzheimer's disease extracellular vesicles were significantly enriched in epitope-specific tau oligomers in comparison to prodromal Alzheimer's disease or control extracellular vesicles as determined by dot blot and atomic force microscopy. Alzheimer's disease extracellular vesicles were more efficiently internalized by murine cortical neurons, as well as more efficient in transferring and misfolding tau, than prodromal Alzheimer's disease and control extracellular vesicles *in vitro*. Strikingly, the inoculation of Alzheimer's disease or prodromal Alzheimer's disease extracellular vesicles containing only 300 pg of tau into the outer molecular layer of the dentate gyrus of 18-month-old C57BL/6 mice resulted in the accumulation of abnormally phosphorylated tau throughout the hippocampus by 4.5 months, whereas inoculation of an equal amount of tau from control extracellular vesicles, isolated tau oligomers, or fibrils from the same Alzheimer's disease donor showed little tau pathology. Furthermore, Alzheimer's disease extracellular vesicles induced misfolding of endogenous tau in both oligomeric and sarkosyl-insoluble forms in the hippocampal region. Unexpectedly, phosphorylated tau was primarily accumulated in glutamic acid decarboxylase 67 (GAD67) GABAergic interneurons and, to a lesser extent, glutamate receptor 2/3-positive excitatory mossy cells, showing preferential extracellular vesicle-mediated GABAergic interneuronal tau propagation. Whole-cell patch clamp recordings of CA1 pyramidal cells showed significant reduction in the amplitude of spontaneous inhibitory post-synaptic currents. This was accompanied by reductions in c-fos$^+$ GAD67$^+$ neurons and GAD67$^+$ neuronal puncta surrounding pyramidal neurons in the CA1 region, confirming reduced GABAergic transmission in this region. Our study posits a novel mechanism for the spread of tau in hippocampal GABAergic interneurons via brain-derived extracellular vesicles and their subsequent neuronal dysfunction.

1 Department of Pharmacology and Experimental Therapeutics, Boston University School of Medicine, Boston, MA 02118, USA
2 Department of Anatomy and Neurobiology, Boston University School of Medicine, Boston, MA 02118, USA
3 Department of Neurology, University of Texas Medical Branch, Galveston, TX 77555, USA
4 Department of Cell Biology, Harvard Medical School, Boston, MA 02115, USA
5 Department of Pharmacology and Experimental Neurosciences, University of Nebraska Medical Center, Omaha, NE 68198, USA
6 Center for Systems Neuroscience, Boston University, Boston, MA 02118, USA
7 Department of Neurology and Alzheimer's Disease Center, Boston University School of Medicine, Boston, MA 02118, USA

Received April 17, 2020. Revised July 29, 2020. Accepted August 17, 2020. Advance access publication November 27, 2020

Correspondence to: Tsuneya Ikezu, MD, PhD
Professor of Departments of Pharmacology and Experimental Therapeutics and Neurology
Boston University School of Medicine, Boston, MA 02118, USA
E-mail: tikezu@bu.edu

Keywords: Alzheimer's disease; extracellular vesicle; GABAergic interneuron; microtubule-associated protein tau; mouse model

Abbreviations: AP = action potential; dfPBS = double-filtered phosphate-buffered saline; EV = extracellular vesicle; KO = knock-out; OML = outer molecular layer; pAD = prodromal Alzheimer's disease; PK = proteinase K; sIPSC = spontaneous inhibitory postsynaptic current; TEM = transmission electron microscopy

Introduction

Accumulation of misfolded microtubule-associated protein tau is a neuropathological hallmark of Alzheimer's disease. The degree of Alzheimer's disease cognitive decline is paralleled by the progression of anatomical spread of misfolded tau (Arriagada *et al.*, 1992). Abnormally aggregated and phosphorylated tau (p-tau) first appears in the entorhinal cortex at the prodromal stage of Alzheimer's disease, spreading in a hierarchical pattern to hippocampal regions and then throughout neocortical areas (Braak and Braak, 1991). A growing body of evidence implicates a prion-like mechanism for this spread of tau. Healthy neurons internalize extracellular tau, which serves as misfolding templates for endogenous tau. The resulting misfolded tau is secreted, continuing this cycle of cell-to-cell transmission of tau.

Extracellular vesicles (EVs), composed of a cell-derived lipid bilayer, are classified as exosomes or microvesicles. Exosomes, which are 30–150 nm in diameter, are secreted after the fusion of endosomes with the cell surface. Microvesicles are 100–1000 nm in diameter and are secreted by the outward budding of plasma membranes (DeLeo and Ikezu, 2018; Ruan and Ikezu, 2019). EVs were originally hypothesized to be part of the clearance system for unmetabolized cell composites. However, recent evidence suggests that EVs play critical roles in the spread of pathological proteins, motivating further investigation of their pathobiology in neurodegenerative diseases (Fevrier *et al.*, 2004; Danzer *et al.*, 2012; Asai *et al.*, 2015; Grad *et al.*, 2015). Tau is secreted primarily in free form, while a minor fraction of tau is found in EVs as observed in the CSF or blood of control subjects and Alzheimer's disease patients (Arai *et al.*, 1998; Saman *et al.*, 2012; Zetterberg *et al.*, 2013; Fiandaca *et al.*, 2015; Ruan and Ikezu, 2019; Brunello *et al.*, 2020). Levels of free tau in the CSF of Alzheimer's disease patients as well as neuron-derived plasma EVs isolated from patients with either mild cognitive impairment or Alzheimer's disease correlated with the progression of disease (Arai *et al.*, 1998; Winston *et al.*, 2016), suggesting potential pathogenic roles of both forms of tau in disease development. It is a matter of debate, however, whether EV-associated and free form tau may contribute differently to tau propagation. A disease-associated role for paired helical filament (PHF)-tau from Alzheimer's disease or other tauopathy brains was demonstrated following its inoculation into mouse brains leading to tau neuropathology (Guo *et al.*, 2016; Narasimhan *et al.*, 2017). Notably, EVs isolated from transgenic tau mouse brains, Alzheimer's disease plasma, or human induced pluripotent stem cells expressing recombinant mutant tau also initiated propagation of tau in mouse brain tissues (Baker *et al.*, 2016; Polanco *et al.*, 2016; Winston *et al.*, 2019). Furthermore, pharmacological inhibition of exosome synthesis significantly reduced tau propagation (Asai *et al.*, 2015; Bilousova *et al.*, 2018). The molecular mechanisms of cell-to-cell transmission of EVs and free tau aggregates via uptake and secretion are subjects of intense investigation (Ruan and Ikezu, 2019; Brunello *et al.*, 2020; Colin *et al.*, 2020). While the mode of neuronal uptake of free tau appears to depend on conformational and post-translational modifications (Mirbaha *et al.*, 2015; Hu *et al.*, 2016; Evans *et al.*, 2018), EV tau uptake is affected by its surface proteins. EVs can target specific cell types by the interaction of their cell surface proteins (van Niel *et al.*, 2018). To understand the molecular composition of human brain-derived EVs, we have recently developed an isolation protocol for human and mouse brain-derived EVs by which we successfully enriched EVs with limited contamination from cytosolic components, including the endoplasmic reticulum and Golgi (Muraoka *et al.*, 2019, 2020*a*). Our proteomic profiling of Alzheimer's disease and control brain-derived EVs identified glia-derived EV molecules enriched in Alzheimer's disease cases; linear discriminant analysis of the EV proteomes could distinguish Alzheimer's disease from control cases with 88% accuracy (Muraoka *et al.*, 2020*a*). Furthermore, EVs isolated from interleukin (IL)-1β-stimulated human primary astrocytes showed increased expression of integrin-β3 (ITGB3), which was critical for enhanced neuronal EV uptake (You *et al.*, 2020). These data demonstrate that disease-associated pathologies, such as glial inflammation, can alter the molecular composition of EVs, affecting their neuronal uptake and potency of tau spread.

There has been no comprehensive analysis of tau pathology development after the injection of human brain-derived EVs from control subjects or Alzheimer's disease patients. Moreover, to fully understand the difference in tau propagation potency between EV-associated and vesicle-free tau, it is critical to compare neuropathology development induced by different forms of tau isolated from the same donor. Herein, we aimed to characterize brain-derived EVs separated from Alzheimer's disease, prodromal Alzheimer's

disease (pAD), and age/sex-matched control subjects for their biophysical, biochemical, and neurobiological properties as well as for tau pathology after their stereotaxic injection into the outer molecular layer (OML) of the dentate gyrus in aged C57BL/6 (B6) mice. The recipient mice were tested by immunohistochemical and biochemical methods for characterization of tau accumulation in the hippocampus. We also assessed the difference in tau pathology development after intrahippocampal injections of isolated EVs, tau oligomers, and tau fibrils in mice. Finally, hippocampal pyramidal neurons of the recipient mice were assessed by whole-cell patch clamp recordings to determine whether tau accumulation induces neurophysiological alterations.

Materials and methods

Animals

Aged C57BL/6 (18–19 months old), tau knockout (KO) (B6.129X1-*Mapt*^{tm1Hnd}/J, # 007251), and pregnant CD-1 mice were purchased from National Institute of Aging (NIA), Jackson laboratory, and Charles River Laboratory, respectively. B6 mice were housed as groups in regular light/dark cycles with free access to food and water, and welfare-related assessments were carried out before and after the surgery. Animals were randomly allocated to experimental groups and variability was assessed based on the body weight. Animals were used for intracerebral inoculation of human brain-derived materials. Adult tau-KO mice were used for isolation of brain-derived EVs. E16 (embryonic Day 16) CD-1 mice were used for primary culture of cortical neurons. All animal procedures followed the guidelines of the National Institutes of Health Guide for the Care and Use of Laboratory Animals and were approved by the Boston University Institutional Animal Care and Use Committee (IACUC).

Isolation of extracellular vesicles from Alzheimer's disease brains

Human and mouse brain-derived EVs were isolated according to our recently published methods (Muraoka *et al.*, 2020*b*), which were adapted from a previous publication (Perez-Gonzalez *et al.*, 2012). Briefly, fresh frozen human frontal cortex was sliced with a razor blade on ice while frozen to generate 2–3 mm^3 sections. The cut sections were dissociated (LK003178, Worthington Biochemical Corporation) in 3 ml Hibernate^{TM}-E medium (Thermo Fisher Scientific) containing 20 units of papain at 37°C for 15 min. After incubation, the samples were immediately added with 6 ml of ice-cold Hibernate^{TM}-E solution (A1247601 Gibco) and filtered using a 40 µm mesh filter (Fisher scientific). The tissue sample was sequentially centrifuged at 300*g* for 10 min at 4°C. The supernatant was transferred to a new 15 ml tube and then centrifuged at 2000*g* for 10 min at 4°C (Eppendorf). This supernatant was then transferred to a 30-ml conical tube and then centrifuged at 10 000*g* for 10 min at 4°C (Avanti J-E JA25-50 Beckman Coulter). The supernatant was filtered through a 0.22 µm pore-size filter (Millipore) and ultracentrifuged at 100 000*g* for 70 min at 4°C using SW41Ti (Optima-XE SW41 Beckman Coulter). The pellet was resuspended in 2 ml of 0.475 M sucrose in double-filtered phosphate-buffered saline (dfPBS) with a 0.22-µm pore-size filter and overlaid on five sucrose cushions (2 ml each of 2.0 M, 1.5 M, 1 M, 0.825 M, and 0.65 M in dfPBS), then ultracentrifuged at 200 000*g* for 20 h at 4°C (Optima-XE SW41 Beckman Coulter). The gradient was collected in 2 ml fractions, where fractions V and VI were enriched in EVs, except for the first and last fractions, which were 1 ml each. EV fractions V and VI were diluted to 12 ml in dfPBS and ultracentrifuged at 100 000*g* for 70 min at 4°C using SW41Ti to pellet EVs, which were finally resuspended in 30 µl dfPBS. The bicinchoninic acid (BCA) assay (Pierce) was used to determine the protein concentration for each sample.

Nanoparticle tracking analysis

The EVs in the enriched fractions were quantified as previously described (Muraoka *et al.*, 2019, 2020*b*). Briefly, all samples were diluted in dfPBS by 1:1000 or greater to be read by the Nanosight 300 (Malvern Panalytical Inc), which can read 10–100 particles per frame. Using a syringe pump infusion system (Harvard Laboratories/Malvern), five 30-s videos of each sample were taken at 21°C. Analysis of particle counts was carried out with Nanosight NTA 3.3 software (Malvern Panalytical Inc), using a detection threshold of five. Particle counts were normalized by the dilution factors for particle reading, the final pellet, and starting material for exosome extraction. Finally, the counts were averaged for fractions V and VI.

Atomic force microscopy

Ten micrograms of EVs (~1 µg/µl) were incubated with 100 µl 0.5% sarkosyl (Sigma-Aldrich) for 30 min on ice in ultracentrifuge-compatible Beckman microcentrifuge tubes for solubilization of vesicles, followed by dilution in dfPBS to 1.2 ml. The sample was ultracentrifuged at 100 000*g* for 70 min at 4°C. The supernatant was removed until 50 µl sample remained, to which dfPBS was added to a volume of 1.2 ml for the second ultracentrifugation at 100 000*g* for 70 min at 4°C. The pellet was dissociated in 10 µl dfPBS and imaged via atomic force microscopy using the Multimode 8 AFM machine (Bruker) under ScanAsyst mode, as previously described (Sengupta *et al.*, 2018).

Tau purification from extracellular vesicles with proteinase K treatment

EVs (90 µg) were diluted to a concentration of 860 µg/ml protein and incubated with 20 µg/ml proteinase K (PK, QIAGEN) and 5 mM $CaCl_2$ in PBS for 1 h at 37°C with gentle vortexing every 15 min. The PK activity was then inhibited by adding 5 mM phenylmethylsulphonyl fluoride (PMSF) for 10 min at room temperature. A quarter volume of each sample was collected for western blot analysis with CD63 and actin antibodies. The rest was lysed with TENT buffer (50 mM Tris HCl pH 7.5, 2 mM EDTA, 150 mM NaCl, 1% Triton^{TM} X-100) (1:1) for 30 min on ice, followed by centrifugation at 48 300*g* for 20 min at 4°C. The supernatant and pellet were designated as S1 and P1 fractions, respectively. The S1 fraction was ultracentrifuged

at 186 000*g* at 4°C for 40 min to collect the pellet fraction (S1p) as the tau oligomer-enriched fraction. The P1 fraction was resuspended in 1 ml of buffer (1% sarkosyl, 10 mM Tris, pH 7.4, 800 mM NaCl, 10% sucrose, 1 mM EGTA, 1 mM PMSF), and incubated by rotating with the benchtop thermomixer at room temperature for 1 h. The sample was ultracentrifuged at 186 000*g* for 1 h at 4°C. After completely removing the supernatant and rinsing the pellet in sterile PBS, the sarkosyl-insoluble pellet (P2), as the tau fibril-enriched fraction, was removed.

Transmission electron and immunoelectron microscopy

Transmission electron microscopy (TEM) of EVs and tau contents purified from human brain-derived EV samples was conducted as previously described (Asai *et al.*, 2015; Muraoka *et al.*, 2020*b*). Briefly, 5 µl of the EV sample was adsorbed for 1 min on a carbon-coated grid (Electron Microscopy Sciences) that had been made hydrophilic by a 20 s exposure to a glow discharge (25 mA). Excess liquid was removed with filter paper (#1 Whatman), then the grid was floated briefly on a drop of water (to wash away phosphate or salt), blotted on filter paper, and then stained with 0.75% uranyl formate (EMS) for 15 s. After removing the excess uranyl formate with a filter paper, the grids were examined in a JEOL 1200EX transmission electron microscope and images were recorded with an AMT 2k CCD camera. For immunogold labelling on tau fibrils, samples were adsorbed to the grid for 5 min, blocked on 1% bovine serum albumin (BSA) for 10 min, transferred to 5 µl drops of primary antibody (PHF1, mouse mAb, 1:10; kindly provided by Dr P. Davies) and incubated for 30 min, then washed in four drops of PBS (total 10 min) before incubation in rabbit anti-mouse bridging antibody (1:50, #ab6709, Abcam) for 30 min followed by 5-nm protein A–gold (University Medical Center, Utrecht, The Netherlands) for 20 min. Grids were washed in two drops of PBS followed by four drops of water (total 15 min) and subsequent staining in 0.75% uranyl formate and imaged as described above. For immunogold labelling on EVs, pelleted exosomes were fixed with 4% paraformaldehyde in 0.1 M phosphate buffer (pH 7.4) and processed for ultrathin cryosectioning. Pellets were infiltrated with 2.3 M sucrose in PBS for 15 min, frozen in liquid nitrogen and sectioned at –120°C. Sections 60–80-nm thick were picked up and transferred to formvar carbon-coated copper grids, and immunogold labelling was carried out at room temperature on a piece of Parafilm. The antibody was diluted in 1% BSA in PBS. Grids were floated on drops of 1% BSA for 10 min to block non-specific labelling, transferred to 5-µl drops of primary antibodies (PHF1, mouse mAb, 1:10) and incubated for 30 min, then washed in four drops of PBS (total 10 min) before incubation in rabbit anti-mouse bridging antibody (1:50, Abcam ab6709) for 30 min followed by 5 nm protein A–gold for 20 min. Grids were washed in two drops of PBS followed by four drops of water (total 15 min) and contrasted in a mixture of 0.3% uranyl acetate in 2% methylcellulose for 5 min. Excess liquid was blotted off with filter paper and the grids were examined at 80 kV with a JEOL 1200EX transmission electron microscope and images were recorded with an AMT 2k CCD camera.

ELISA of brain tissue extraction and extracellular vesicle samples

Brain tissue homogenate and EV samples were diluted 1:10 in 8 M guanidine buffer for solubilization for 3 h at room temperature with agitation, followed by dilution in TENT buffer supplemented with protease and phosphatase inhibitors (Pierce HALT inhibitor), and subjected to human total tau ELISA (Thermo Fisher Scientific) according to the manufacturer's instructions.

Extracellular vesicle labelling with PKH26

EVs were labelled with lipophilic red fluorescent dye (PKH26, Sigma-Aldrich), according to the manufacturer's protocol. Briefly, 0.32 µl PKH26 was mixed with 5 µg EV samples in 40 µl diluent C, and incubated for 5 min at room temperature. dfPBS was used as a negative control. The labelling reaction was stopped by adding 50 µl chilled dfPBS, and subjected to Exosome Spin Columns (MW 3000, ThermoFisher) at 750*g* for 2 min to remove the free dye and enrich the labelled EVs, which were adjusted to 5 µg/100 µl for the neuronal EV uptake assay.

Primary tissue culture of murine cortical neurons

Primary murine cortical neurons were isolated from E16 embryos from pregnant CD-1 mice (Charles River Laboratory). Dissociated cortical tissues were digested with trypsin-EDTA (diluted to 0.125%, Invitrogen), triturated with polished pipettes, strained into single neurons using a 40-µm pore-size Falcon cell strainer (Thermo Fisher Scientific), and finally plated onto sterilized 12-mm high precision thickness coverslips (Bioscience Tools) at 375 000 cells per coverslip in 24-well plates, as previously described (You *et al.*, 2020). Coverslips were precoated with 100 µg/ml poly-D-lysine (Sigma-Aldrich) diluted in borate buffer (0.05 M boric acid, pH 8.5) and washed with sterile water prior to plating. Neurons at day *in vitro* 7 were treated with PKH26-labelled EVs for neuronal uptake or tau transfer study.

Tau seeding assay

HEK-TauRD P301S Förster resonance energy transfer (FRET) biosensor cells (ATCC) were plated on a poly-D-lysine-coated 96-well plate (# 354461, Corning) in growth media (Dulbecco's modified Eagle medium, 10% foetal bovine serum, 1× penicillin/streptomycin, all from Invitrogen). The next day, human brain-derived EVs were mixed with 80 µl Opti-MEM and 20 µl Lipofectamine™ 2000, and incubated at room temperature for 10 min. Subsequently, growth media was removed from the cells, replaced with samples containing Lipofectamine, and incubated at 37°C, 5% CO_2. After 1 h, Lipofectamine-containing media was removed from the cells and replaced with growth media. Cells were maintained in culture at 37°C, 5% CO_2 for 72 h afterward. The day of the analysis, cells were washed in PBS, detached with 0.25% Trypsin-EDTA (Invitrogen), and washed with the fluorescence-activated cell sorting (FACS) buffer (PBS + 0.5% BSA). Subsequently, cells were fixed in 2% paraformaldehyde, 2% sucrose solution in PBS for 15 min at 4°C, spun at 13 500*g* for 15 min at 4°C, then resuspended in

FACS buffer. FRET assays were performed with LSRII flow cytometer (BD Bioscience) using pacific-orange and pacific-blue dye filter settings for yellow and cyan fluorescent protein, respectively. Data were analysed using FlowJo and quantified as integrated FRET density.

Stereotaxic surgery

C57BL/6 mice at 18–19 months old were deeply anaesthetized with isoflurane and immobilized in a mouse stereotaxic frame (David Kopf Instruments) installed with robotic stereotaxic injection system (Drill and Injection Robot, Neurostar). Animals were unilaterally inoculated with human or tau-KO mouse brain-derived EVs, or tau aggregates purified from Alzheimer's disease human brain in the dorsal hippocampal OML (bregma: –2.18 mm; lateral: 1.13 mm; depth: –1.9 mm from the skull) using a 10-µl Hamilton syringe. Each injection site received 1.0 µl of inoculum, containing 300 pg tau/µl for EV samples, saline, 300 pg or 2 µg of tau per microlitre oligomers or fibrils, and euthanized 4.5 months after the injection. We noted that the majority of injected materials were deposited at the OML of the hippocampus (Fig. 4A).

Immunochemistry and immunofluorescence

Brains were removed after transcardial perfusion fixation with ice-cold 4% paraformaldehyde/PBS followed by post-fixation for 16 h and cryoprotection with 15%, then 30% sucrose/PBS over 3–5 days, and embedded in O.C.T. compound (Thermo Fisher). They were cryosectioned coronally in 20-µm thickness using a cryostat, and three hippocampal sections separated by at least 200 µm per mouse were used for immunohistochemistry per primary antibody. The sections were processed by antigen retrieval with Tris-EDTA (pH 8.0) at 80°C, permeabilized in 0.5% Triton™ X-100/PBS, and blocked in 10% normal goat serum, 1% BSA, and 0.1% Tween-20 in PBS, as previously described (Asai *et al.*, 2015). Sections were incubated with primary antibodies against glutamic acid decarboxylase 67 (GAD67, PA5-36054, ThermoFisher Scientific), GAD67-biotin-conjugated (MAB5406B, Millipore), parvalbumin (PV, ab11427, Abcam), neurogranin (Ab5620, Millipore Sigma), $pSer^{202}$/$pSer^{205}$ tau (AT8, MN1020, ThermoFisher Scientific), GluR2/3 (AB1506, Millipore Sigma), MAP-2 (mab3418, Millipore Sigma), c-fos (226003, Synaptic Systems), $pSer^{422}$ tau (PS422, 44-764G, ThermoFisher Scientific), along with misfolded tau (Alz50 and MC1), $pSer^{202}$ tau (CP13) and $pSer^{396}$/$pSer^{404}$ tau (PHF-1, all kind gifts provided by Dr Peter Davies), diluted with 1% BSA, 0.025% Tween-20 in PBS at 4°C overnight (see Supplementary Table 1 for antibody dilution information). Sections were then washed and incubated in secondary antibodies (Alexa Fluor 647 goat anti-mouse; 1:1000, Alexa Fluor 488 goat anti-rabbit; 1:1000, Alexa Fluor 568 streptavidin 1:1000) for 1 h at room temperature. All images were captured on Nikon deconvolution wide-field epifluorescence system (Nikon Instruments) or confocal microscopic imaging, as described below.

Confocal image processing and quantification by Imaris

All confocal imaging was performed on a LSM710 using Zen 2010 software (Zeiss) or a Leica TCS SP8 lightning microscope on an inverted Leica DMi8 microscope stand, using the confocal mode for 63× oil immersion/1.4N.A objective, and 1.1 optical zoom at a pinhole of 1.0 airy unit. Confocal stacks of images with 2048 × 2048 pixel resolution were collected while using a system-optimized *z*-interval of 0.28 µm. $GAD67^+$ puncta were imaged with a 552 nm laser, and emission was collected at 565–650nm; for imaging c-fos, a 488 nm laser line was used and emission was collected at 490–600 nm. All co-localization images were scanned frame-by-frame in the sequential scanning mode, which showed no cross-talk among multiple channels. Gain and offset were set at values which prevented saturated and empty pixels. All images were processed via adaptive LIGHTNING deconvolution (Leica) after image acquisition. The quantification of $GAD67^+$ puncta was counted using the 'Spot' module of Imaris 9.5, 64-bit version (Bitplane AG). CA1 pyramidal cells were manually cut with GAD67 field in 3D. This program analyses stacks of confocal sections acquired in two channels (red for GAD67, blue for DAPI represents the nuclei). Final data analysis was performed with Excel (Microsoft) and Prism 8 (GraphPad).

Biochemical sequential extraction from mouse brains

Brain tissues were removed from control EV, pAD EV and Alzheimer's disease EV-injected mice at the designated time points after transcardial perfusion of animals by ice-cold PBS to minimize contamination of blood-derived mouse immunoglobulins. Hippocampal and cortical regions were dissected separately, snap-frozen in dry ice, and stored at –80°C before protein extraction. For enrichment of tau oligomers and fibrils, sequential extractions were performed as follows: each hippocampal tissue was homogenized in nine volumes of TBS buffer (50 mM Tris-Cl, pH 8.0 in saline) and supplemented with protease and phosphatase inhibitor cocktails (Thermo Fisher Scientific). The homogenate was centrifuged at 48 300*g* for 20 min at 4°C. The supernatant and pellet were designated as S1 (TBS-supernatant) and P1 (TBS-pellet) fractions, respectively. The S1 fraction was ultracentrifuged at 186 000*g* at 4°C for 40 min. The pellet fraction (S1p) was resuspended in 10 µl PBS and frozen at –80°C as the tau oligomer-enriched fraction. The P1 fraction was resuspended in five volumes of wet weight of the original tissue of buffer B (1% sarkosyl, 10 mM Tris, pH 7.4, 800 mM NaCl, 10% sucrose, 1 mM EGTA, 1 mM PMSF, all from Sigma-Aldrich), and incubated by rotating with the benchtop thermomixer at room temperature for 1 h. The sample was ultracentrifuged at 186 000*g* for 1 h at 4°C. After completely removing the supernatant and rinsing the pellet in sterile PBS, sarkosyl-insoluble pellet (P2) was resuspended with 10 µl PBS, and frozen at –80°C as tau fibril-enriched fraction.

Western and dot blotting

For EV samples, after being lysed with TENT buffer, the equivalent amount of protein was loaded on 4–20% SDS-PAGE gels (Bio-Rad). For mouse brain tissue samples, homogenates of

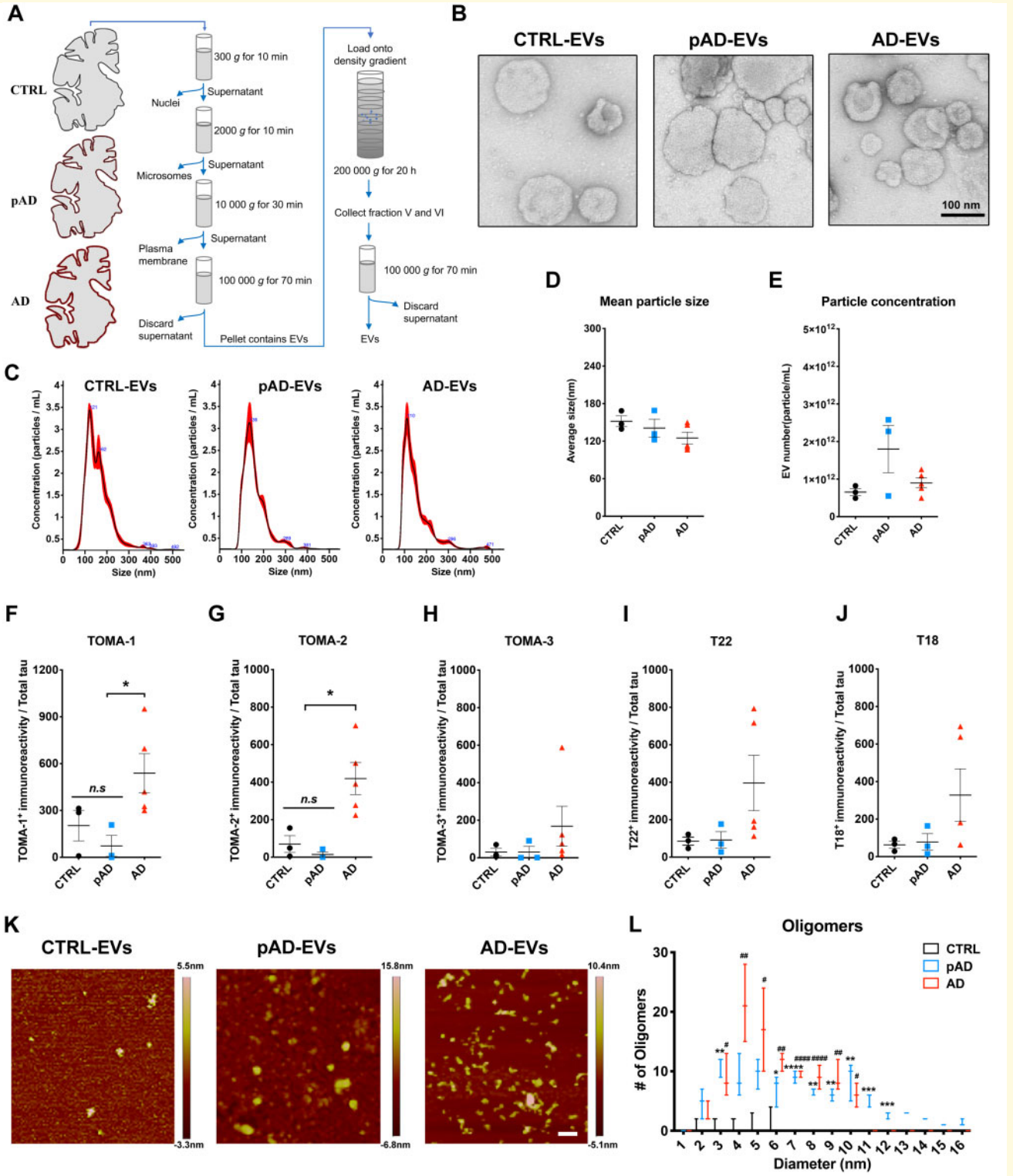

Figure 1 Characterization of EVs by TEM, nanoparticle tracking analysis, tau oligomer dot-blotting and atomic force microscopy. (**A**) A schema of EV separation from human frozen brain tissue. (**B**) TEM image of human brain-derived EVs. (**C**–**E**) Nanoparticle tracking analysis of isolated EVs (**C**), quantification of EV size (**D**) and EV density (**E**). (**F**–**J**) Semi-quantification of tau oligomers in EVs by multiple tau oligomer antibodies. Dot blot images are provided in Supplementary Fig. 1A. $^{*}P < 0.05$, as determined by one-way ANOVA (alpha = 0.05) and Tukey's *post hoc*. Graphs indicate mean ± SEM. Each dot represents an individual donor, three replicates per subject, three donors per group for control (CTRL) and pAD, five donors for the Alzheimer's disease (AD) group (Supplementary Table 2). (**K** and **L**) Atomic force microscopy images showing brain-derived EV-tau oligomers isolated from CTRL, pAD, and Alzheimer's disease brains (**K**). Scale bars = 200 nm. Size distribution histogram of EV-tau oligomers (**L**). $^{*}P < 0.05$, $^{**}P < 0.01$, $^{***}P < 0.005$ and $^{****}P < 0.0001$ for pAD EVs versus CTRL EVs; $^{\#}P < 0.05$, $^{\#\#}P < 0.01$, and $^{\#\#\#\#}P < 0.0001$ for Alzheimer's disease EVs versus CTRL EVs as determined by one-way ANOVA (alpha = 0.05) and Tukey's *post hoc*. Graphs indicate mean ± SEM. n = 3 images per sample. AD = Alzheimer's disease; CTRL = control.

hippocampus from each experimental group and an equal proportion of corresponding homogenates, S1, S1p and P2, were loaded on 10% SDS-PAGE gels (Bio-Rad) and electrotransferred to 0.45 μm nitrocellulose membranes (Bio-Rad). For dot blotting, an equal volume of EV samples were dotted onto 0.45 μm nitrocellulose membranes (Bio-Rad) and washed twice with TBS buffer. The membranes were then blocked in freshly prepared 5% BSA diluted in TBS before being immunoblotted with specific primary antibodies (Supplementary Table 1). The membrane was further incubated with HRP-labelled secondary antibodies (Santa Cruz Biotech) and scanned using the C300 digital chemiluminescent imager (Azure Biosystems). The band densities were digitally measured using ImageJ (NIH).

Whole-cell patch clamp recording

Preparation of brain slices for recording and filling

Immediately after decapitation, mouse brains were rapidly removed and placed in oxygenated (95% O_2 and 5% CO_2) ice-cold Ringer's solution containing the following ingredients (in mM): 25 $NaHCO_3$, 124 NaCl, 1 KCl, 2 KH_2PO_4, 10 glucose, 2.5 $CaCl_2$, 1.3 $MgCl_2$ (pH 7.4; Sigma-Aldrich). A total of four to five 300-μm thick acute coronal sections containing the hippocampus were obtained from each subject. Over an 8–10-h period, slices were individually transferred from the incubation chamber to submersion-type recording chambers (Harvard Apparatus) affixed to the stages of Nikon E600 infrared-differential interference contrast (IR-DIC) microscopes (Micro Video Instruments) with a water-immersion lens (40×, 0.9 NA; Olympus) for recording. During recordings, slices were superfused in room-temperature Ringer's solution bubbled with carbogen (95% O_2, 5% CO_2) at a rate of 2.5 ml/min. Whole-cell patch clamp recordings were obtained from the soma of visually identified CA1 pyramidal cells in both the dorsal and ventral hippocampus of the ipsilateral side of the brain. Electrodes were created from borosilicate glass with a Flaming/Brown micropipette puller (Model P-87, Sutter Instruments). These pulled patch pipettes were filled with potassium methanesulphonate (KMS)-based intracellular solution, with concentrations in mM as follows: (KCH_3SO_3 122, $MgCl_2$ 2, EGTA 5, Na-HEPES 10, Na_2ATP 5). Each had a resistance of 5.5–6.5 MΩ in external Ringer's solution.

Physiological inclusion criteria

Single action potential (AP) properties [including threshold, amplitude, action potential half-width (APHW), rise and fall] were measured on the second evoked AP in a 200 ms current-clamp series that preferentially evoked three or more APs after depolarizing step-current. We proceeded to high input resistance or low input resistance only if neurons were unable to elicit AP at 200 ms. APHW was computed at half-max of AP amplitude, where the amplitude was measured from the threshold to the absolute peak of the spike. All quantification of AP properties was carried out in an expanded timescale, using the linear measure tool from FitMaster analysis software (HEKA Elektronik). An algorithm designed in MATLAB was used to automatically detect these parameters. In the few cases where it failed to do so, a manual detection method was used. The final paradigm in the current-clamp configuration was to inject 2 s hyperpolarizing and depolarizing steps (–100 to +120 pA with increments of 20 pA or –220 pA to +330 pA with increments of 50 pA, 12.5 kHz sampling frequency) to assess repetitive AP firing. Those neurons that did not fire repetitively during the depolarizing step were discarded. Firing rates in response to current steps were determined by fitting to a generalized linear model, using the genotype, CA1 pyramidal cells types, rheobase, input resistance, injected current level, and their respective interactions as independent variables. Whole-cell voltage clamp was used to measure AMPA receptor-mediated spontaneous excitatory currents (sEPSCs) response for 2 min at a holding potential of –80 mV (6.67 kHz sampling frequency). The same neuron was held at –40 mV (6.67 kHz sampling frequency) for 2 min to obtain enough sample size to measure GABA receptor-mediated spontaneous inhibitory currents (sIPSCs). All recorded traces were run through Mini Analysis Program (Synaptosoft), which allowed for quantification of synaptic current properties such as frequency, amplitude, area, time to rise, and time to decay. To determine the kinetics of EPSCs and IPSCs, the rise and decay of averaged traces were each fit to a single-exponential function. In all of the synaptic current measurements, the event detection threshold was set to the maximum root mean squared noise level (5 pA). All neurons had resting membrane potentials between –55 and –75 mV (somatic recordings) and were confirmed to have intact somas and apical tufts by fluorescence microscopic imaging of biocytin-filled cells.

Statistical analyses

All data are presented as means ± standard error of the mean (SEM). Comparisons between two groups were done by two-tailed paired or unpaired Student's *t*-tests. Multiple comparisons were performed by either one- or two-way ANOVA, followed by Tukey's or Bonferroni's *post hoc* test. Statistical analyses were performed using Prism 8.0 (GraphPad). A statistically significant difference was assumed at $P < 0.05$.

Data availability

The authors confirm that the data supporting the findings of this study are available within the article and its Supplementary material.

Results

Detection of tau oligomers in Alzheimer's disease brain-derived extracellular vesicles

While tau has been found in both exosomes and microvesicles in tauopathy mouse brains, neuroblastoma cells, and the CSF and plasma in Alzheimer's disease patients (Arai *et al.*, 1998; Saman *et al.*, 2012; Dujardin *et al.*, 2014; Fiandaca *et al.*, 2015), there has been no study to date which reports a detailed analysis of control, pAD, and Alzheimer's disease brain-derived EVs. To this end, we isolated exosome-enriched EV fractions from Alzheimer's disease, pAD, and control subject brain samples (three cases per group, see Supplementary Table 2 for demographics) and tau-KO mouse brain tissues (Supplementary Table 2) using a combination of high-speed

centrifugation, filtration, discontinuous sucrose gradient ultracentrifugation, and additional ultracentrifugation, as recently published (Muraoka *et al.*, 2020*a*, *b*) (Fig. 1A). Analysis of the isolated fractions by TEM (Fig. 1B) and nanoparticle tracking analysis (NTA, Fig. 1C) demonstrated enrichment of brain EVs in the exosome size range (Budnik *et al.*, 2016). There was no difference in terms of EV particle concentration or size among groups (Fig. 1D and E). We detected total tau and amyloid-β_{42} but not amyloid-β_{40} in EVs by ELISA. Amyloid-β_{42} was significantly enriched in Alzheimer's disease EVs compared to pAD or control EVs (Supplementary Table 3). Considering that the tau oligomer is roughly a nanometer in size (Combs *et al.*, 2017), we postulated that brain-derived EVs contain tau in oligomeric form. Indeed, there was a significantly higher amount of oligomeric tau in EVs derived from Alzheimer's disease compared to controls as determined by dot blotting of tau oligomer-specific monoclonal antibodies TOMA-1 and TOMA-2, but not by TOMA-3 (Fig. 1F–H and Supplementary Fig. 1). There was no difference in immunoreactivity to tau oligomer polyclonal antibodies T22 and T18 among three patient groups (Fig. 1I and J). In addition, atomic force microscopy analysis showed that the detergent-insoluble fraction of Alzheimer's disease and pAD, but not of control EVs, contained significantly more globular particles at a mode height of 4–6 nm, consistent with tau oligomers (Fig. 1K and L). Taken together, these data suggest that Alzheimer's disease and pAD EVs are enriched in tau oligomers compared to control subjects, suggesting their EV tau seeding potency and pathogenic activities.

Detection of sarkosyl-insoluble tau aggregates within Alzheimer's disease extracellular vesicles

To determine whether the tau is inside or associated with EVs, we first treated EV samples with PK to digest EV-associated proteins, which has been used in EV-related studies. PK can digest proteins on the outer leaflet of EVs, such as CD9 and CD63, but does not digest the luminal proteins, such as Tsg101 and actin (Cvjetkovic *et al.*, 2016). In our study, we also determined which form of tau in EVs is

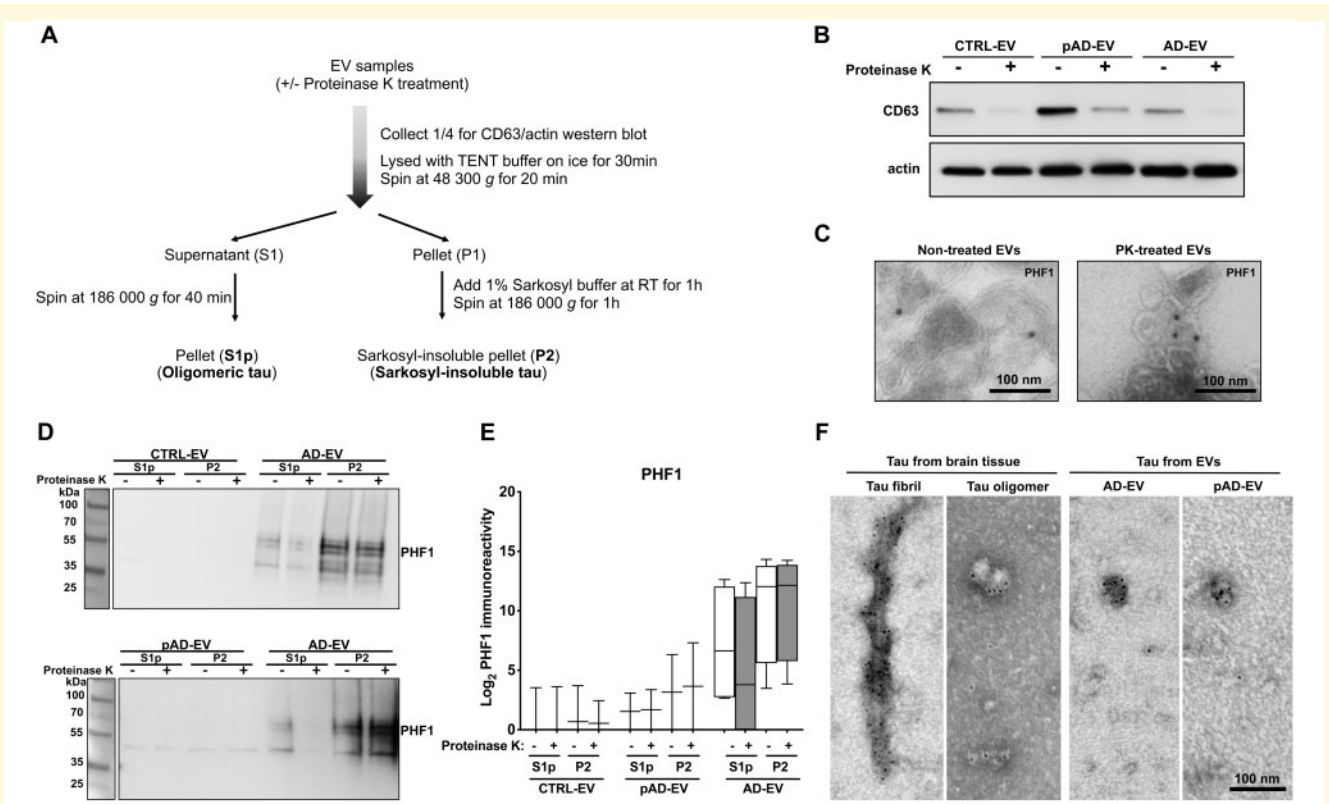

Figure 2 PK treatment of human brain derived EVs for biochemical characterization. (**A**) Workflow of the tau purification by sequential centrifugation after with or without PK treatment. (**B**) Western blot analysis of non-treated and PK-treated EVs from three groups (CTRL, pAD and Alzheimer's disease) with CD63 and actin antibodies. (**C**) Immunoelectron microscopy images of ultrathin-sectioned Alzheimer's disease EVs for PHF1$^+$ tau with or without PK-treatment. Images were captured at direct magnification $\times$30 000, with the 10 nm immunogold labelling. (**D**) Western blot analysis of oligomer-enriched (S1p) and sarkosyl-insoluble tau-enriched (P2) fractions from EVs for PHF1 with or without PK-treatment. (**E**) Semi-quantification of PHF1 immunoreactivity. Two donors per group for CTRL and pAD and four donors for the Alzheimer's disease group. (**F**) Immunoelectron microscopy of isolated tau fibrils, oligomers or sarkosyl-insoluble fraction of EVs from human Alzheimer's disease brain tissue. Images were captured by TEM at direct magnification $\times$40 000, with the 5-nm immunogold labelling for PHF1. (**A**–**F**) Donors 1 and 2 (control, CTRL), 4 and 5 (pAD), and 7–10 (Alzheimer's disease, AD) were used (Supplementary Table 2).

enriched by sarkosyl solubilization and sequential centrifugation of lysed EVs to separate the oligomer-enriched fraction (S1p) and sarkosyl-insoluble fraction (P2) using control, pAD, and Alzheimer's disease EVs containing the same amount of protein per sample (Fig. 2A). PK treatment successfully reduced the amount of CD63 in all the EV samples (control, pAD, and Alzheimer's disease) as a positive control, but did not affect the amount of actin within EVs as a negative control (Fig. 2B). Immunoelectron microscopic analysis shows that PK treatment did not significantly change detection of EVs with PHF1 monoclonal antibody, which detects pS^{396}/pS^{404} tau (Fig. 2C). Furthermore, $PHF1^+$ tau is mostly enriched in the P2 fraction in Alzheimer's disease EVs, while $PHF1^+$ tau was also detected in the S1p fraction (Fig. 2D and E). PK treatment did not affect the P2 tau in Alzheimer's disease EV samples while it partially reduced the S1p tau. $PHF1^+$ tau was almost undetectable in control and pAD EV samples (Fig. 2D and E).

To observe the structure of tau in the human brain-derived EV samples, we lysed Alzheimer's disease and pAD EVs with 2% sarkosyl buffer and ultracentrifuged to isolate the sarkosyl-insoluble fraction of tau aggregates. As controls, tau oligomers and fibrils were isolated by sarkosyl solubilization and sequential centrifugation/ultracentrifugation from the same Alzheimer's disease brain tissues. The isolated samples were subjected to immunoelectron microscopy with PHF1 and immunogold. As shown in Fig. 2F, we detected a $PHF1^+$ paired helical structure in isolated tau fibril and globular structures of tau oligomers as the control. Interestingly, we detected mostly $PHF1^+$ globular structures in both Alzheimer's disease and pAD EVs (Fig. 2F), likely representing oligomer or protofibril tau. Taken together, these data show that $PHF1^+$ tau detected in Alzheimer's disease EVs are mostly inside the EVs in a sarkosyl-insoluble globular form, whereas the tau oligomer form can also be associated with the outer-leaflet of EVs. $PHF1^+$ tau was detectable at a much lower level in the S1p and P2 fractions in a PK-insensitive manner, while it was undetectable in either fraction of the control EVs.

Detection of neuronal and glial molecules in brain-derived extracellular vesicles

We have previously reported enrichment of glial molecules and reduction in neuronal molecules in Alzheimer's disease EVs (Muraoka *et al.*, 2020*a*). To validate these findings from proteomics analysis, we performed western blot with several cell type-specific proteins identified from the proteomic profiling of the brain-derived EV samples (Muraoka *et al.*, 2020*a*). Interestingly, we detected myelin oligodendrocyte glycoprotein (MOG), a mature oligodendrocyte marker, as being significantly more enriched in the Alzheimer's disease EV samples than in pAD or control EV samples (Supplementary Fig. 2A and B), consistent with the proteomics data. For astrocyte-specific markers, we tested excitatory amino acid transporter 1 (EAAT1), glial fibrillar acidic protein (GFAP), and aquaporin-4 (AQP4). We observed a trend of enrichment of EAAT1, but reduction of GFAP in pAD or Alzheimer's disease EVs compared to control EVs, whereas AQP4 showed no difference (Supplementary Fig. 2A and C). For neuron-specific markers, synaptophysin (SYP) showed a significant decrease in the Alzheimer's disease EV samples compared to the control EV samples, along with a similar trend in L1 cell adhesion molecule (L1CAM) band intensity (Supplementary Fig. 2A and D), consistent with the proteomics data. The discrepancy observed in astrocytic markers could be due to the limitation of the quantification by label-free proteomic mass spectrometry, which depends on the quantitative comparisons using the label-free intensity-based absolute quantification (iBAQ) method with all samples normalized by total ion current for the run. Taken together, these findings suggested that more glia- and less neuron-derived molecules are enriched in the Alzheimer's disease EVs.

Increased uptake of Alzheimer's disease extracellular vesicles by neurons and subsequent tau transfer

Protein-protein interactions between EVs and cell surface molecules of recipient cells can facilitate the binding of EVs and subsequent endocytosis (Mulcahy *et al.*, 2014; van Niel *et al.*, 2018). We hypothesized that Alzheimer's disease-induced inflammatory brain conditions affect the efficiency of EV uptake by altering molecular complexes of the EV's surface. Therefore, we investigated the efficiency of the brain-derived EV uptake by primary cultured murine neurons *in vitro*. After 7 days of neuronal differentiation, the cells were incubated with PKH26-labelled EVs isolated from the brain tissue of Alzheimer's disease, pAD, and control samples over 24 h, as previously described (You *et al.*, 2020) (Fig. 3A). Alzheimer's disease EVs showed significantly higher neuronal uptake compared to control EVs, but there was no significant change between pAD and control EV groups (Fig. 3B and C). The transfer efficiency of tau from EV to neurons was significantly higher in Alzheimer's disease EVs compared to that of control EVs (Fig. 3D). We labelled the supernatant with PKH26 as a negative control at the last ultracentrifugation wash step of the EV isolation and applied it to neuronal cells. There was no PKH26 positivity found in supernatant applied neurons (data not shown). Finally, to understand if EV-tau has different tau seeding activity dependent on the disease conditions, we used a FRET-based tau seeding assay, as previously described (Holmes *et al.*, 2014). Astonishingly, the Alzheimer's disease EVs showed significantly higher seeding activity compared to the pAD and control EV groups (Fig. 3E), suggesting higher potency of Alzheimer's disease EVs to induce tau pathology. In summary, the data demonstrate the pathogenic functions of

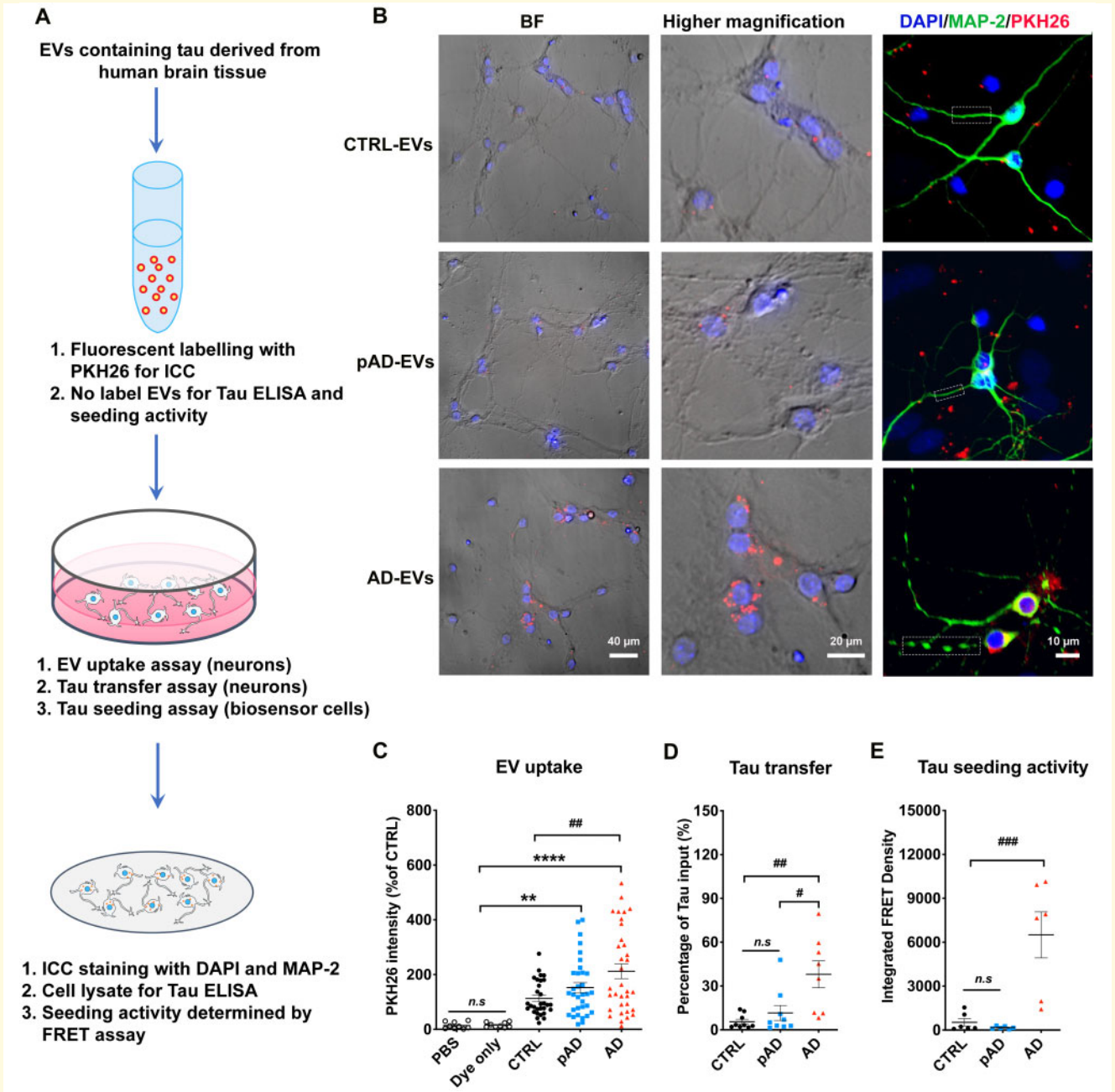

Figure 3 Neuronal uptake, tau transfer efficiency and tau seeding activities of human brain-derived EVs. (**A**) A diagram illustrating the primary culture model with primary neurons used to measure the transfer of EVs containing tau and a biosensor cell assay system for seeding activity. (**B**) Cellular uptake of PKH26-labelled EVs (red) by primary culture murine cortical neurons (MAP-2, green; DAPI, blue). Original magnification: ×20 (*left* and *middle* columns); 40× (*right* column, taken by Zeiss LSM710 confocal microscopy). Scale bars = 40, 20, 10 μm (*left* to *right*). (**C**) Quantification of PKH26 fluorescent intensity in neurons. $^{**}P < 0.0001$ and $^{****}P < 0.0001$ compared with PBS or dye only group; $^{\#\#}P < 0.01$ compared with the CTRL-EV group; determined by one-way ANOVA (alpha = 0.05) and Tukey's *post hoc*. Each dot represents average data per image (10–20 cells per image), nine images per group (for PBS and dye only), 10 images per donor and three donors per group (for control EV, pAD EV, and Alzheimer's disease EVs), total *n* = 30 per group. (**D**) Total human tau ELISA of neuronal cell lysates. $^{\#}P < 0.05$ compared with pAD EV and $^{\#\#}P < 0.01$ compared with the control EV group; n.s denotes no significance as determined by one-way ANOVA (alpha = 0.05) and Tukey's *post hoc*. Three donors per group, three independent experiments. Graphs indicate mean ± SEM. (**E**) EVs were tested in the tau-FRET assay for tau seeding activity. Results are plotted as integrated FRET density values for each sample. $^{\#\#\#}P < 0.001$ compared with control EV and pAD EV groups; as determined by one-way ANOVA (alpha = 0.05) and Tukey's *post hoc*. Three donors per group, and each dot represents one well. Graphs indicate mean ± SEM. (**B**–**E**) Donors 1–3 (control), 4–6 (pAD), and 7–9 (Alzheimer's disease) were used (Supplementary Table 2). AD = Alzheimer's disease; BF = bright-field; CTRL = control; FRET = Förster resonance energy transfer; ICC = immunocytochemistry.

Alzheimer's disease EVs with efficient neuronal uptake, tau transfer, and tau seeding potency.

Inoculation of Alzheimer's disease extracellular vesicles propagates tau pathology in aged mice

We further investigated whether brain-derived EVs can initiate tauopathy *in vivo* using 2-month-old B6 mice. Brain-derived EVs isolated from the brain tissue of Alzheimer's disease, pAD, and control cases were unilaterally injected in the OML of the dentate gyrus (Fig. 4A). The amount of injected tau (300 pg/µl, 1 µl per injection) was much lower than that used in previous tau propagation studies (1–8 µg) (Guo *et al.*, 2016; Narasimhan *et al.*, 2017). The concentration was in the range of the extracellular tau concentration in mouse interstitial fluid of the CNS (Yamada *et al.*, 2014). Immunofluorescence against $pSer^{202}$/$pSer^{205}$ tau (AT8) yielded a considerable, yet not abundant amount of $AT8^+$ cells in the hippocampal region of Alzheimer's disease and pAD EV-injected female mice (Supplementary Fig. 3), while Alzheimer's disease and pAD EV-injected male mice show no AT8 positivity (data not shown). A previous study reported enhancement of tau propagation induced by tau fibril injection in aged B6 mice in comparison to young mice (Guo *et al.*, 2016). Therefore, we tested aged female mice as recipients to determine whether tau pathology induced by brain-derived EVs reflects the donor's disease conditions. Brain-derived EVs were isolated from three donors each of Alzheimer's disease, pAD, and control cases, with tau-KO mouse brain-derived EVs serving as a negative EV control. Each EV sample (containing 300 pg tau/injectate for human brain-derived EVs or saline control), was unilaterally injected into the OML of the dentate gyrus of 18–19-month-old B6 female mice (Fig. 4A). The spread of tau pathology was evaluated by immunofluorescence against AT8 in the hippocampal region at 4.5 months post-injection (Fig. 4B and Supplementary Figs 3 and 4A). Interestingly, abundant perikaryal $AT8^+$ inclusions were detected in both ipsilateral and contralateral sides of the hippocampal region including the CA1, CA3, dentate granule cells, subgranular zone, and hilus, in the Alzheimer's disease and pAD EV groups, suggesting that tau transfers between anatomically connected pathways (Fig. 4B). Semiquantitative brain-wide mapping of tau pathologies revealed that $AT8^+$ pathogenic tau was accumulated throughout the hippocampus, and was predominantly distributed in the caudal hilus region in the mouse brains injected with Alzheimer's disease or pAD EVs, while control EV injected mouse brains showed very little AT8 positivity (Fig. 4C). Notably, the percentage of the area occupied by $AT8^+$ cells in the hippocampal region was significantly higher in Alzheimer's disease EVs compared to the control EV, saline, or tau-KO EV groups (Fig. 4D). There was no significant difference between pAD and control EV injected groups, and no $AT8^+$ staining was observed in the saline or tau-KO injected groups (Fig. 4D and Supplementary Fig. 4A). All $AT8^+$ neurons were negative for human tau, as determined by immunofluorescent staining against human tau-specific monoclonal HT7 (data not shown), indicating that endogenous mouse tau was recruited and aggregated by the inoculation of human brain-derived EV tau. A growing body of evidence suggests that misfolded tau tends to be truncated and frequently consists of different conformers or structural polymorphisms, dependent on the stages and disease of tauopathy (Fitzpatrick *et al.*, 2017; Falcon *et al.*, 2018, 2019; Sigurdsson, 2018; Zhang *et al.*, 2020). Therefore, we performed neuropathological analysis of tau by immunohistochemistry using conformation-specific (Alz50 and MC1) and p-tau epitope-specific monoclonal antibodies (CP13 for $pSer^{202}$ tau, PS422 for $pSer^{422}$ tau, and PHF1 for $pSer^{396}$/$pSer^{404}$ tau). All five antibodies detected misfolded or phosphorylated tau mainly in the hilus of hippocampal region of Alzheimer's disease and pAD EV groups (Supplementary Fig. 4B–F).

We next examined whether EV-tau could induce templated misfolding of original tau aggregates in the endogenous tau of the recipient mice. Aggregated tau was extracted from the recipient mouse brains via sarkosyl solubilization and sequential centrifugation, and immunoblotted using Tau-5 and PHF1 monoclonal antibodies, as previously described (Fig. 4E) (Apicco *et al.*, 2018; Jiang *et al.*, 2019). We observed a significant increase in oligomeric tau in the S1p fraction of both Alzheimer's disease and pAD EV injected mouse hippocampi in comparison to the control EV group, determined by both Tau-5 (total tau) and PHF1 immunoblotting (Fig. 4F and G). The amount of sarkosyl-insoluble tau in the P2 fraction was also significantly elevated in Alzheimer's disease EV injected mouse hippocampi when compared to the control EV group (Fig. 4F and G). These data indicate that Alzheimer's disease EV inoculation induced accumulation of oligomeric and fibrillar tau, while pAD EV inoculation induced accumulation of oligomeric tau. Taken together, these data show the efficient induction of tau propagation in the hippocampus of the aged B6 female mouse brain after the OML injection of Alzheimer's disease EVs containing a physiological concentration of tau. Conformational changes of tau in the recipient mice appear to reflect the original tau conformation of Alzheimer's disease EVs and pAD EVs, which was also reported in mice injected with Alzheimer's disease brain-derived tau fibrils (Guo *et al.*, 2016).

Extracellular vesicles propagate more tau than tau oligomers or fibrils when injected into mouse brains

To determine how propagation of tau pathology may differ between the injection of EV-associated or free form tau, we compared EV tau with oligomeric and fibrillar tau derived from the same donor for tau pathology development. Oligomeric and fibrillar tau was isolated from the same Alzheimer's disease EV donor as the S1p and P2 fractions according to the previous publications (Guo *et al.*, 2016; Apicco *et al.*, 2018; Jiang *et al.*, 2019). The p-tau immunoreactivity and structure of the isolated tau aggregates were

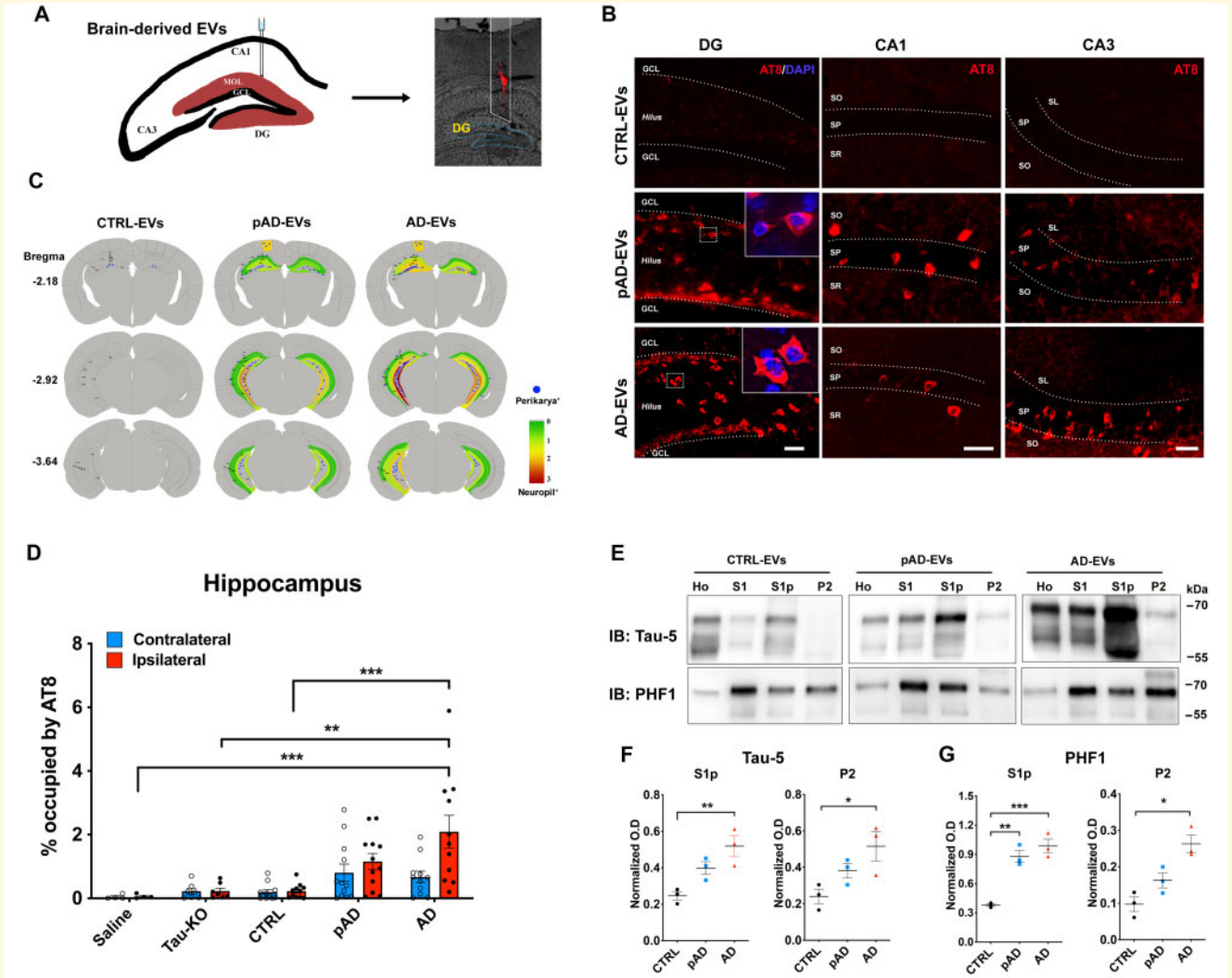

Figure 4 Alzheimer's disease EV but not control EV injection causes progressive tauopathy in aged B6 mouse brains. (**A**) A schema illustrating 300 pg of tau containing EVs from human brain unilaterally injected to the hippocampus of B6 mice at 18–19 months of age. DiI (red) indicated the injection site of the OML of the hippocampus. (**B**) Representative image of AT8 staining (red) 4.5 months after intrahippocampal injection of Alzheimer's disease EV and pAD EV into aged B6 mouse brain. Original magnification: ×20. Scale bar = 50 μm. (**C**) Semi-quantitative analysis of Alzheimer's disease-like tau pathologies based on AT8 immunostaining of brains from control, pAD, and Alzheimer's disease (AD) EV-injected mice at 4.5 months post-injection. Blue dots represent $AT8^+$ perikaryal inclusions. $AT8^+$ density from green (0, low) to red (3, high). (**D**) Quantification of $AT8^+$ occupied area in the contralateral (blue) and ipsilateral (red) in entire hippocampal regions of recipient mice. $^{**}P < 0.01$ and $^{***}P < 0.001$ compared with the control EV group determined by one-way ANOVA (alpha = 0.05) and Tukey's *post hoc*. Total mice in each group for the quantification were 4, 6, 12, 12, and 11 for saline, tau-KO, control, pAD, and Alzheimer's disease. Two donors for EVs per group for control (Donors 1 and 2), pAD (Donors 4 and 5), and Alzheimer's disease (Donors 7 and 9), (n = 5–6 mice per donor). Bregma –1.34 to –3.64, four sections per mouse were analysed. Each dot represents mean value from one animal. Graphs indicate mean ± SEM. (**E**) Immunoblotting of biochemically fractionated brain tissue samples for homogenate (Ho), TBS supernatant (S1), tau oligomer enriched (S1p) and tau fibril enriched fractions (P2) by Tau-5 (total tau) and PHF1 (pSer396/pSer404 tau) (*top*) and their quantification (*bottom*). Equal proportions of homogenate (Ho), S1, S1p, and P2 fractions were analysed (n = 3 mice/group). Optical density (OD) was normalized to that for the homogenate fraction from each corresponding mouse. $^{*}P < 0.05$, $^{**}P < 0.01$ and $^{***}P < 0.001$ compared with the control group as determined by one-way ANOVA (alpha = 0.05) and Tukey's *post hoc*. Graphs indicate mean ± SEM. CTRL = control; DG = dentate gyrus; IB = immunoblot.

examined by western blot using a PHF1 antibody and atomic force microscopy (Fig. 5A and B). The atomic force microscopy images showed mostly small, oligomeric, globular particles (6–8 nm in height) in EV and tau oligomer preparations, and large, globular structures (30–70 nm in height) in sonicated tau fibril preparations (Fig. 5A), which is consistent with the description of the fibril structure as previously reported (Ghag *et al.*, 2018). We observed a mainly monomeric $PHF1^+$ band in p-tau in EV and tau oligomer enriched samples, and a trimeric $PHF1^+$ band in fibril

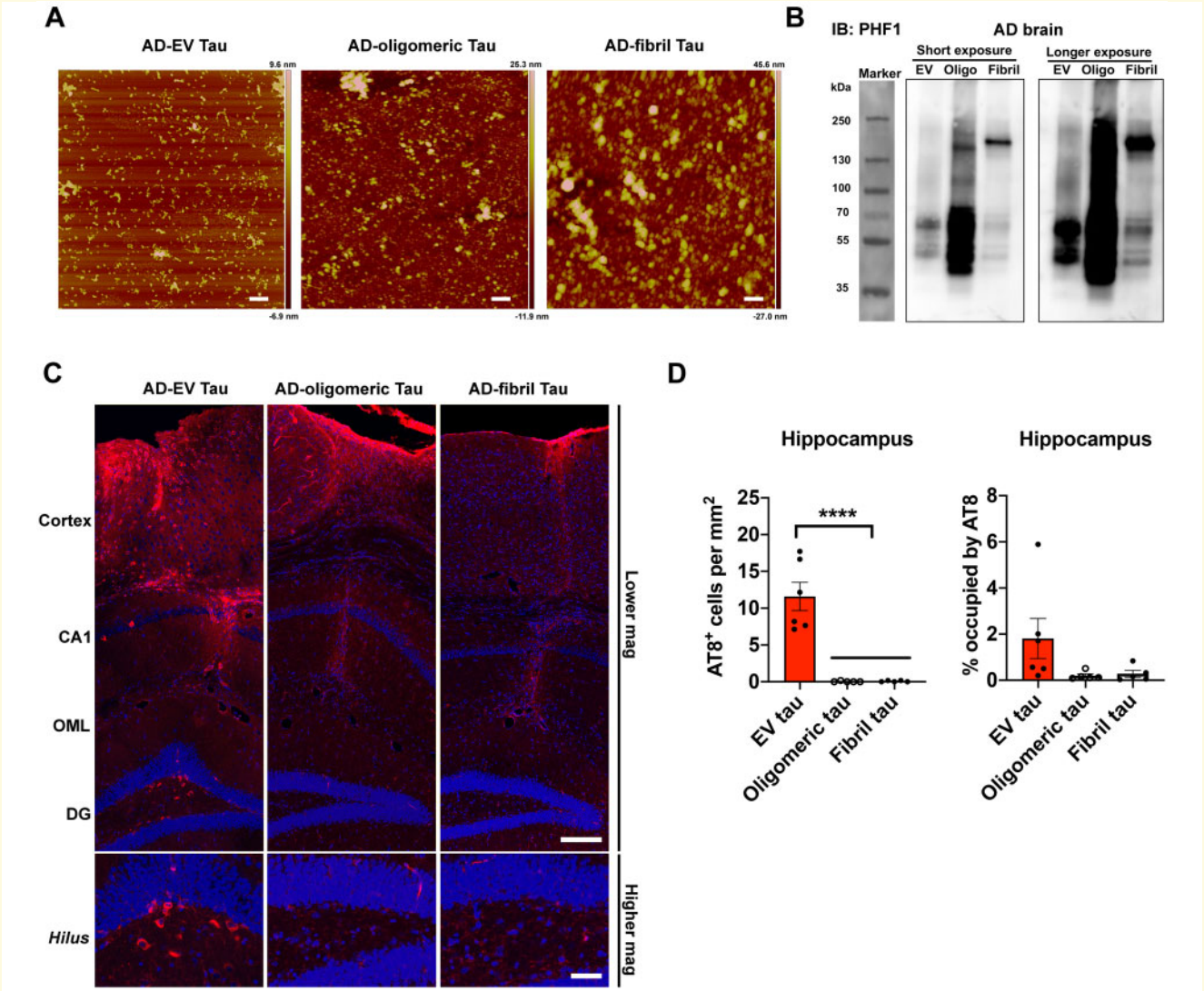

Figure 5 EV-tau but not oligomeric or fibrillar tau enriched samples derived from the same Alzheimer's disease brain induced tau propagation in mouse brain. (**A**) Atomic force microscopy images of EVs and tau aggregates isolated from the same Alzheimer's disease (AD) brain tissues. Scale bars = 200 nm. (**B**) Representative images of PHF1 immunoblotting of isolated EVs, tau oligos and tau fibrils by PHF1 antibody. (**C**) Representative images of AT8 immunostained recipient mice after unilateral injection of Alzheimer's disease EVs (*left*), tau oligomer-enriched fraction (*middle*) and tau fibril-enriched fraction (*right*) in cortical region (*top*) and dentate gyrus (DG, *bottom*). Scale bars = 200 μm (*top*), 50 μm (*bottom*). (**D**) Quantification of $AT8^+$ neurons in the hippocampus of recipient mice. $^{****}P < 0.0001$ compared between EV-tau injected group and oligomeric or fibril tau group, as determined by one-way ANOVA (alpha = 0.05) and Tukey's *post hoc*. EV-tau, oligomeric, and fibril tau group: $n = 5$–6 mice per group for quantification. Bregma –1.34 to –3.64, four sections per mouse were analysed. Each dot represents mean value per animal. Graphs indicate mean ± SEM. (**A**–**D**) Donor 7 was used (Supplementary Table 2). IB = immunoblot.

enriched samples (Fig. 5B), validating their oligomeric and fibrillar conformation. We injected each sample of Alzheimer's disease EVs, oligomers, and fibrils containing an equivalent amount of tau (300 pg/1 μl injectate) into the OML of the dentate gyrus of 18-month-old B6 female mice. At 4.5 months after the injection, mice were tested for tau pathology by immunofluorescence against AT8. We observed strong AT8 positivity in the injection site with all groups, suggesting successful intrahippocampal injections. Whereas only neuropil accumulation of tau along the needle tract was observed in oligomeric or fibrillar tau injected mice (Fig. 5C and Supplementary Fig. 5), which is in agreement with the previous study (Guo *et al.*, 2016), we found $AT8^+$ signal as perikaryal inclusions or neuropil staining in the cortex with EV-tau injected mice (Fig. 5C and Supplementary Fig. 5). Moreover, compared to the $AT8^+$ tau pathology observed in the entire hippocampal region in Alzheimer's disease EV injected mice as previously described, oligomeric or fibrillar tau injected mice did not show any $AT8^+$ perikaryal inclusions in the entire hippocampus (Fig. 5C and D). Consistent with previous reports (Guo *et al.*, 2016), injection of 2 μg of oligomer or fibril tau from

the same Alzheimer's disease brain tissues in aged B6 mice induced robust tau pathology in the hippocampal region, thus providing the fidelity of our oligomeric or fibrillar tau isolation methods (Supplementary Fig. 6A–C). These findings recapitulated our previous study showing that inoculation of microglia-derived EVs containing 5 ng of aggregated tau, but not inoculation of an equal amount of free tau aggregates, was able to induce tau propagation in the dentate gyrus of B6 mice (Asai *et al.*, 2015). Previous studies reported that inoculation of 1–8 μg of fibril tau from Alzheimer's disease patients into wild-type (B6 and B6/C3H F1) mouse brains could induce tau propagation as early as 3 months post-injection (Guo *et al.*, 2016; Narasimhan *et al.*, 2017). Potency of propagation may vary between the donors and the type of tauopathies (Narasimhan *et al.*, 2017), therefore making it difficult to compare the results between these studies. To the best of our knowledge, this is the first report of efficient tau propagation potency in EV-tau in comparison with vesicle-free tau (either oligomer or fibril-enriched fraction) isolated from the same human Alzheimer's disease brain tissue.

Preferential extracellular vesicles mediate tau propagation to GABAergic interneurons

Recent studies have claimed that enriched proteins on the surface of EVs determine the specific type of organs and cells to which the EVs may be transferred (van Niel *et al.*, 2018). For example, previous studies found that specific EV proteins, such as integrins or tetraspanins, play critical roles in the delivery of cancer-derived EVs to specific organs or cell types (Nazarenko, 2010; Hoshino *et al.*, 2015). Given that some proteins are specifically expressed on Alzheimer's disease EVs (Muraoka *et al.*, 2020*a*), we speculated that EV-mediated transfer of tau to aged mouse brains would have cell type specificity. For that purpose, we performed double immunostaining using antibodies against p-tau (AT8) and GABAergic interneurons [GAD67 and parvalbumin (PV)] or excitatory neurons [neurogranin (NG), and glutamate receptor 2/3 (GluR2/3)] (Volz *et al.*, 2011). Surprisingly, most AT8$^+$ cells were GAD67$^+$ interneurons in the CA1, CA3, and dentate gyrus regions in the Alzheimer's disease and pAD EV groups (Fig. 6A and B). Moreover, a subset of PV$^+$ neurons were also co-localized with AT8 (Supplementary Fig. 7A). We found that the ratio of GAD67$^+$AT8$^+$ cells over total GAD67$^+$ cells was significantly higher in the dentate gyrus regions of Alzheimer's disease EV and pAD EV groups compared to the control EV group. This significance was also found in the CA1 and CA3 regions of the Alzheimer's disease EV group compared to the control EV group (Fig. 6C–E). However, there was no significant reduction in the total number of GAD67$^+$ neurons in those regions among the three groups. No difference in the total number of GAD67$^+$ neurons was observed in any of the regions between the tau-KO and control EV groups. In contrast, no NG$^+$ excitatory neurons were AT8$^+$ in the dentate gyrus of the hippocampus (Supplementary Fig. 7B). However, we observed that some AT8$^+$ cells were GluR2/3$^+$ mossy cells in the hilus region (Fig. 6F). Quantification of AT8$^+$ cells in the hippocampal region in the Alzheimer's disease EV group revealed that 64% and 23% of the AT8$^+$ cells were GAD67$^+$ interneurons and GluR2/3$^+$ excitatory mossy cells, respectively (Fig. 6G). Together, our data demonstrate that EVs may play a critical role in tau propagation to GABAergic interneurons, and suggest that EVs can be an attractive therapeutic target for the early intervention of Alzheimer's disease.

Extracellular vesicle inoculation reduces GABAergic interneuronal activity and input to CA1 pyramidal cells

To determine whether EV-mediated tau propagation may disrupt GABAergic interneuronal functions, we examined the neuronal activity of GAD67$^+$ cells by immunofluorescence against c-fos. There was a significant reduction in c-fos$^+$/GAD67$^+$ cells in the CA1 region of the Alzheimer's disease EV group compared to the tau-KO EV group (Fig. 7A and C). However, there was no difference in the number of c-fos$^+$/GAD67$^+$ cells in the dentate gyrus between any groups (Fig. 7B and D), suggesting regional difference in GABAergic interneuronal activity by EV-mediated tau propagation. We further assessed the synaptic input of GABAergic interneurons to CA1 pyramidal cells by quantifying the number of GAD67$^+$ puncta surrounding CA1 pyramidal neuronal cell soma. The images were captured by confocal microscope and the number of the puncta was analysed by Imaris software (Fig. 7E). There was a significant reduction in the number of GAD67$^+$ puncta in the CA1 pyramidal layer of the pAD EV group, and a decreased tendency in the Alzheimer's disease EV group compared to the tau-KO EV group (Fig. 7F). There was no difference in the cell numbers of CA1 pyramidal neurons among groups (Fig. 7G). CA1 pyramidal neurons receive abundant inhibitory inputs from GABAergic interneurons (Caraiscos *et al.*, 2004). Therefore, our results suggest a possible dysregulated function in CA1 pyramidal neurons via disrupted GABAergic interneuronal function after EV-mediated tau propagation.

Extracellular vesicles alter intrinsic membrane properties and spontaneous inhibitory synaptic currents

To evaluate the functional effect of tau propagation in human brain-derived EV-inoculated mouse brains, we performed whole-cell voltage/current-clamp recordings of CA1 pyramidal cells using 300-μm thick acute tissue slices of mouse hippocampi from the tau-KO, pAD, and Alzheimer's

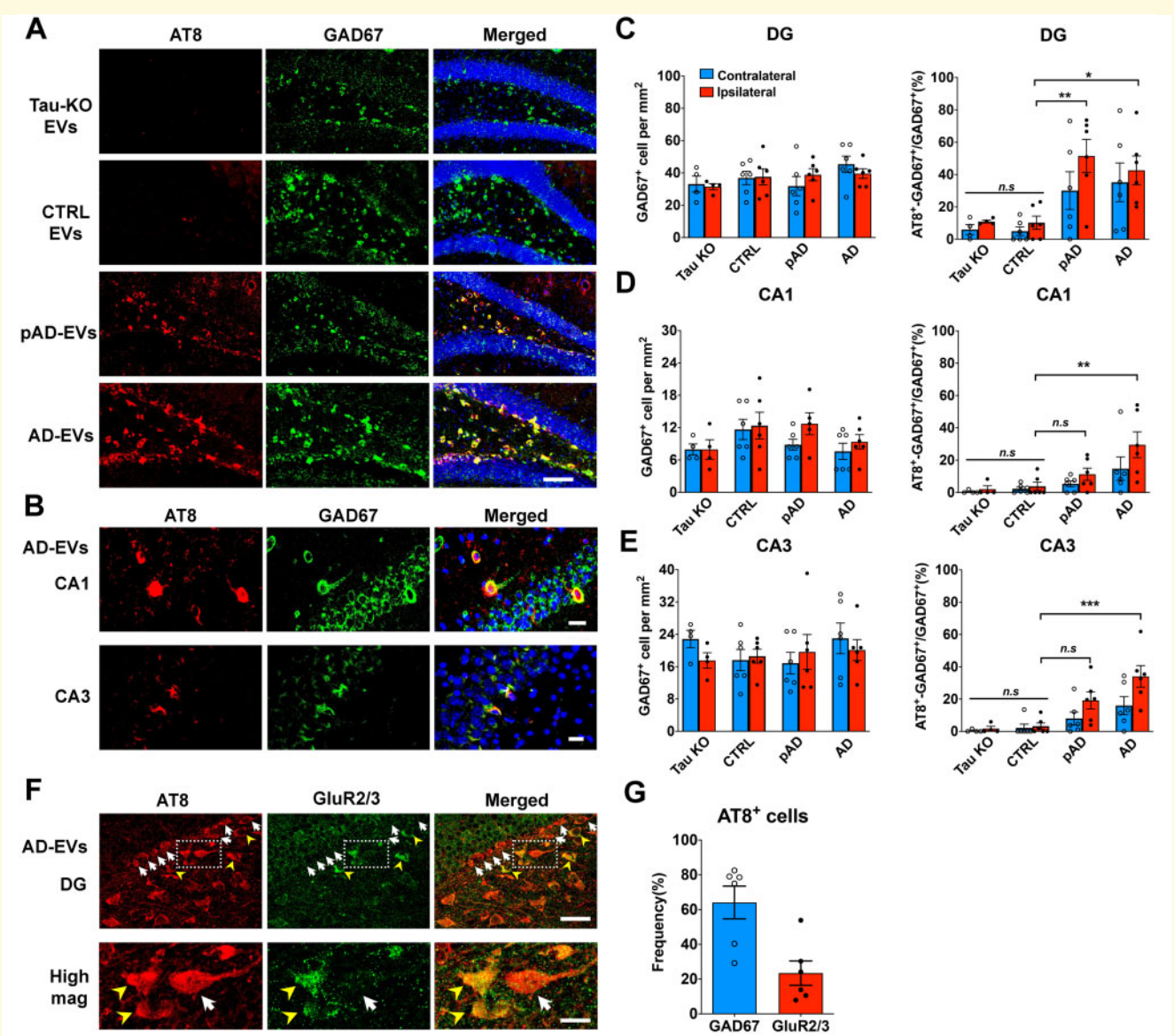

Figure 6 Specific pathological tau staining with AT8 antibody in GABAergic interneurons in the hippocampus of B6 mice. (**A**) AT8 (red) and GAD67 (green) immunostaining in the ipsilateral dentate gyrus (DG) of hippocampal region from tau-KO EV, control EV, pAD EV, and Alzheimer's disease (AD) EV injected mice at 4.5 months post-injection. Scale bars = 100 μm. (**B**) AT8 (red) and GAD67 (green) immunostaining in the ipsilateral CA1 and CA3 of hippocampal region from Alzheimer's disease EV injected mice. Scale bars = 20 μm (*top*), 25 μm (*bottom*). (**C**–**E**) Quantification of GAD67$^+$ cells in dentate gyrus (**C**), CA1 (**D**), and CA3 of hippocampus (**E**). The percentage of AT8$^+$ GAD67$^+$ cells in all GAD67$^+$ cells are shown in the *right* column (**C**–**E**). Ipsilateral side (red column) contralateral side (blue column)*$P < 0.05$, **$P < 0.01$ and ***$P < 0.001$ compared with control group, as determined by one-way ANOVA (alpha = 0.05) and Tukey's *post hoc*. n = 5–6 mice per group for quantification. At least two sections were imaged per animal. Each dot represents mean value per animal. Graphs indicate mean ± SEM. (**F** and **G**) Immunostaining of GluR2/3$^+$ mossy cells (**F**) and AT8 in the ipsilateral dentate gyrus of hippocampal region from Alzheimer's disease EV injected mice; and quantification of the ratio of GAD67$^+$ AT8$^+$ cells/total AT8$^+$cells (blue) and GluR2/3$^+$ AT8$^+$ cells/AT8$^+$ cells (red) (**G**). n = 6 mice per group for quantification. At least two sections were imaged per animal. Each dot represents mean value per animal. Graphs indicate mean ± SEM. Scale bars = 20 μm (*top*), 10 μm (*bottom*). (**A**–**G**) Control (Donors 1 and 2), pAD (Donors 4 and 5), and Alzheimer's disease (Donors 7 and 9) were used (Supplementary Table 2). CA1/3 = cornu ammonis 1/3; CTRL = control.

disease EV groups (Fig. 8A and B). An F-I curve-generating protocol ranging from –100 pA to +120 pA square pulse current steps (increments of +20 pA) or –220 pA to +330 pA current steps (increment of +50 pA) was applied. The number of APs evoked by the depolarizing current steps was significantly lower in the pAD and Alzheimer's disease EV groups than the tau-KO EV group, as determined by repeated measurement ANOVA (Fig. 8C, E and Supplementary Tables 4 and 5). This significantly lowered number of APs also continued for the pAD EV group

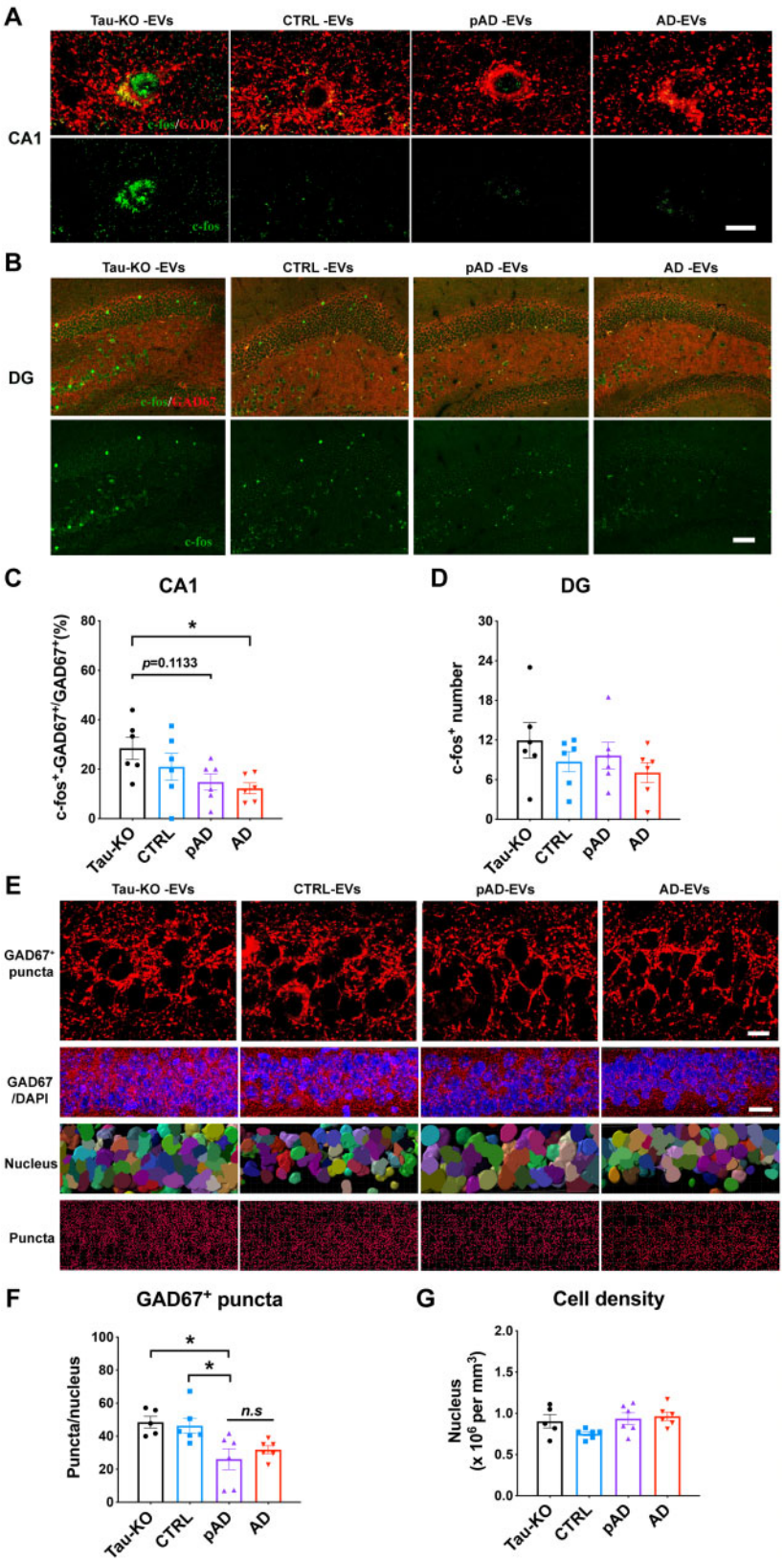

Figure 7 Reduction in c-fos expression in GAD67$^+$ GABAergic interneurons and GAD67$^+$ puncta around CA1 pyramidal cells in Alzheimer's disease EV and pAD EV injected aged B6 mice. (**A**–**D**) GAD67 (red) and c-fos (green) co-staining images and quantification of the percentage of c-fos$^+$ GAD67$^+$ cells in all GAD67$^+$ cells in CA1 region (**A** and **C**) and total c-fos$^+$ positive cells in the dentate gyrus (DG) region (**B** and **D**). Scale bar = 10 μm (**A**), 50 μm (**B**). *$P < 0.05$ Alzheimer's disease EVs compared with the tau-KO EV group, as determined by one-way ANOVA (alpha = 0.05) and Tukey's *post hoc*. $n = 6$ mice per group for quantification. At least two sections were imaged per

(continued)

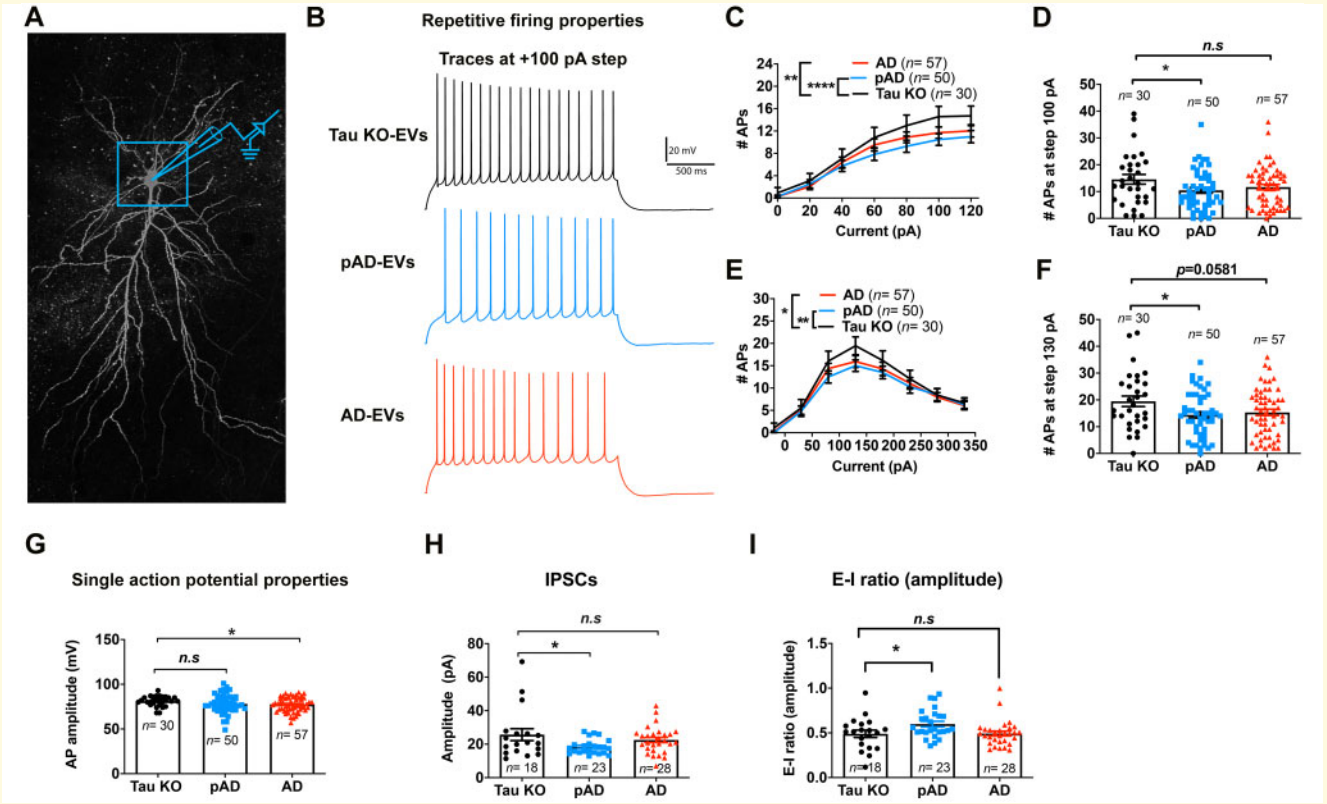

Figure 8 Whole-cell patch clamp recording of CA1 pyramidal neurons. (**A**) Confocal z-stack montage (× 63 magnification) image of biocytin-filled mouse CA1 pyramidal neurons after recording. (**B**–**G**) AP-firing recorded in whole-cell current clamp mode. (**B**) Representative traces for tau-KO (black colour), pAD (blue colour), and Alzheimer's disease EV (red colour) for 100 pA steps at 2-s long high input resistance protocol. (**C**) Quantification of repetitive firing at high input resistance step current injection protocol. $^{**}P < 0.01$ Alzheimer's disease EV versus tau-KO EV, $^{****}P < 0.0001$ as group as determined by two-way ANOVA; (**D**) pAD EV significantly reduce the firing at 100 pA, $^{*}P < 0.05$ pAD EV versus tau-KO EV as determined by one-way ANOVA. (**E**) Quantification of repetitive firing at high input resistance step current injection protocol. $^{*}P < 0.05$ Alzheimer's disease EV versus tau-KO EV, $^{**}P < 0.01$ as group as determined by two-way ANOVA. (**D**) pAD EV significantly reduce the firing at 130 pA, $^{*}P < 0.05$ pAD EV versus tau-KO EV as determined by one-way ANOVA. (**G**) Alzheimer's disease EVs significantly reduced AP amplitude, $^{*}P < 0.05$ Alzheimer's disease EV versus tau-KO EV, as determined by one-way ANOVA. (**C**–**G**) n = 30, 50, and 57 cells for tau-KO, pAD, and Alzheimer's disease (AD) EV injected mice, respectively; n = 5–7 mice per group. Each dot represents one recorded cell. Graphs indicate mean ± SEM. (**H** and **I**) Quantification of GABAergic sIPSCs recorded in whole-cell voltage clamp mode from neuronal network. The pAD group showed a significant decrease in sIPSC amplitude (**H**) and E-I amplitude ratio (**I**). $^{*}P < 0.05$ as compared with the control group, as determined by one-way ANOVA (alpha = 0.05) and Dunnett's *post hoc*. (**H** and **I**) n = 18, 23, and 28 cells for tau-KO, pAD and Alzheimer's disease-EV injected mice, n = 5–7 mice per group. Each dot represents one recorded cell. Graphs indicate mean ± SEM. (**A**–**I**) Donors 1, 4 and 7 were used (Supplementary Table 2). See also Supplementary Tables 4–7.

Figure 7 Continued

animal. Each dot represents mean value per animal. Graphs indicate mean ± SEM. (**E**) High magnification images in *top* panels compared GAD67 expression (red) in CA1 pyramidal cells of the hippocampus in all four injected tau-KO, control, pAD or Alzheimer's disease (AD) EV groups. Scale bar = 10 μm. *Second* panel shows lower magnification images of GAD67 expression and DAPI staining. Scale bar = 20 μm. *Third* panel shows cells counted by Imaris software based on DAPI staining. *Bottom* panel shows $GAD67^{+}$ puncta analysis by Imaris. Scale bar = 10 μm. (**F** and **G**) Quantification of $GAD67^{+}$ puncta (**F**) and total cell number in CA1 of hippocampus (**G**). $^{*}P < 0.05$, pAD EV compared with tau-KO and control EV groups, as determined by one-way ANOVA (alpha = 0.05) and Dunnett's *post hoc*. n = 5–6 mice per group for quantification. At least two sections were imaged per animal. Each dot represents mean value per animal. Graphs indicate mean ± SEM. (**A**–**G**) Control (Donors 1 and 2), pAD (Donors 4 and 5), and Alzheimer's disease (Donors 7 and 9) were used (Supplementary Table 2).

compared to the tau-KO EV group at +100 pA ($P = 0.0434$) and +130 pA ($P = 0.0445$) (Fig. 8D and F). This result is consistent with the study on another tau transgenic mouse model (aged rTg4510 mice expressing P301L tau), which shows reduction in firing of hippocampal CA1 neurons (Hatch *et al.*, 2017). The Alzheimer's disease EV group also showed significant reduction of mean AP amplitude compared to the tau-KO EV group (Fig. 8G). Evaluation of the properties of sIPSCs and sEPSCs (Fig. 8H and Supplementary Tables 6–8) revealed a significant reduction in the mean amplitude of sIPSCs and E-I ratio of amplitude in the pAD EV group compared to the tau-KO group (Fig. 8H and I). There was no difference in sEPSC properties among the three groups. Taken together, these data demonstrate a reduction in AP firing rates of CA1 pyramidal neurons in the pAD EV group, reduction of AP amplitude in the Alzheimer's disease EV group, and reduction in sIPSC amplitude in the pAD EV group, which is also reflected in the reduction in the E-I ratio of sIPSC amplitude. These diverse changes in intrinsic and synaptic properties in Alzheimer's disease and pAD EV groups indicate that CA1 pyramidal cell function is impacted in a variety of functionally relevant ways, likely downstream to the effects of tau accumulation in GABAergic interneurons, which modulate the activity of pyramidal cells.

Discussion

The current study demonstrates that Alzheimer's disease EVs efficiently initiate tau propagation in aged B6 mice. This finding was validated *in vitro* by their higher uptake by cortical neurons and increased seeding activity compared to control EVs. Tau pathology was predominantly found in GABAergic interneurons, and to a lesser extent in the mossy cells in the dentate gyrus. Whole-cell patch clamp recordings of CA1 pyramidal cells in recipient mice showed reduced intrinsic excitability and lower mean sIPSC amplitude, indicative of intrinsic dysfunction of CA1 pyramidal cells and reduced input from interneurons. This was accompanied by a reduction in inhibitory synaptic markers and c-fos immunoreactivity in GABAergic interneurons in the CA1 region. The preferential EV-mediated tau propagation into GABAergic interneurons and their reduced function posits the potential underlying mechanism for interneuron dysfunction in Alzheimer's disease.

Extracellular vesicles mediated neurodegenerative disease progression

Recent advances in EV research have opened new avenues to investigate the diagnostic and pathogenic roles of EVs on neurodegenerative diseases (Delpech *et al.*, 2019; You and Ikezu, 2019). The evidence now suggests that EVs carry pathogenic proteins, and EV-associated proteins or miRNAs predict disease progression in Alzheimer's disease (Cheng *et al.*, 2015; Winston *et al.*, 2016), chronic traumatic encephalopathy (Stern *et al.*, 2016), Parkinson's disease, prion disease, amyotrophic lateral sclerosis, traumatic brain injury, multiple sclerosis, and Huntington's disease (Delpech *et al.*, 2019). Furthermore, overexpression of the second most Alzheimer's disease-associated genome-wide associated study (GWAS) gene, bridging integrator 1 (*BIN1*), enhanced release of tau via EVs *in vitro* and exacerbated tau pathology in PS19 mice *in vivo* (McAvoy *et al.*, 2019). However, because of the scarcity of tau in the EV fractions of biofluids, the contribution of EVs to tau pathology development in Alzheimer's disease patients has been questioned. We have demonstrated here that mice injected with physiological levels of free-form tau, either oligomers or fibrils, showed vastly diminished propagation in comparison to mice injected with physiological levels of EV-associated tau. EVs containing only 300 pg of tau successfully induced templated misfolding in endogenous tau and subsequently transferred tau pathology through the entire hippocampus in aged B6 mice, indicating that EVs are indeed vehicles capable of transferring pathological tau.

A previous study reported that immunodepletion of tau from Alzheimer's disease brain-derived tau fibrils diminished tau aggregation activity *in vitro* or propagation *in vivo* (Guo *et al.*, 2016). Moreover, addition of the remaining components into the Alzheimer's disease-tau depleted sample did not alter the outcomes of the aforementioned experiments, suggesting that tau, but not tau-associated molecules, was the essential component to initiate tau propagation (Guo *et al.*, 2016). Our results also indicate that neither EVs without tau (tau-KO EVs) nor control EVs containing less tau aggregates than Alzheimer's disease EVs initiate tau propagation *in vivo*. However, we have confirmed that EVs certainly enhance the propagation potency of tau by showing lack of tau pathology development after the injections of 300 pg of tau oligomers or fibrils without EVs. Application of sarkosyl to brain samples during the tau fibril purification step can lyse the EVs, thus the isolated tau fibril may contain both free form tau and EV-derived tau aggregates, which can also contribute to the tau propagation and be immunodepleted by the anti-tau antibody. Our TEM and biochemical analyses show that tau is associated with the EV surface as well as contained inside EVs. Therefore, the discrepancy between these experiments may be due to the potential removal of EVs associated with extracellular tau when immunodepletion of tau was performed. Moreover, the amount of intact EVs in the remaining components used for the injection is undetermined, and the EV structure is likely disturbed by the sarkosyl treatment.

Higher transmissibility of Alzheimer's disease extracellular vesicles

Alzheimer's disease EVs show higher transmissibility of tau via increased uptake by recipient neurons. EV surface

proteins are known to interact with receptors on cell membranes, and such interactions are a key component to determine the efficiency of EV uptake. For example, integrin family proteins on EVs have been shown to interact with intercellular adhesion molecules (ICAMs) (Morelli *et al.*, 2004) or fibronectin and laminin proteins of the extracellular matrix on recipient cell surfaces (Sung *et al.*, 2015; Purushothaman *et al.*, 2016; van Niel *et al.*, 2018). Heparin sulphate proteoglycan (HSPG) (Christianson *et al.*, 2013) and galectin (Barres *et al.*, 2010) have also been studied for their regulation on EV uptake. EV surface protein repertoires are known to reflect their biological condition and cell-type specificity of parental cells (Im *et al.*, 2014; van Niel *et al.*, 2018). Our recent proteome of human brain-derived EVs revealed that control EVs expressed more proteins of neuronal origin, while Alzheimer's disease EVs showed more glial dominance (Muraoka *et al.*, 2020*a*). This may reflect the neuroinflammatory condition recently described as the third core Alzheimer's disease pathogenesis following amyloid-β plaques and neurofibrillary tangles (Kinney *et al.*, 2018). Interestingly, recent analysis of single cell RNAseq of human Alzheimer's disease brains showed that CD81, an established tetraspanin exosome marker, is highly expressed in the microglia module (Mathys *et al.*, 2019) together with *APOE*, the most prominent Alzheimer's disease GWAS gene (Lambert *et al.*, 2009). Notably, APOE has been shown in separate studies to regulate activation of microglia in neurodegenerative diseases (Keren-Shaul *et al.*, 2017; Krasemann *et al.*, 2017). These findings suggest active EV and APOE synthesis in microglia in Alzheimer's disease brains. Furthermore, CD81 and CD82 are known to regulate the integrin cluster distribution on plasma membranes to facilitate dendritic cell adhesions (Quast *et al.*, 2011) and recruit integrins to the endosomal pathway (He *et al.*, 2005), respectively. In addition, our recent study demonstrates that IL-1β-stimulated astrocytes secrete EVs enriched in the integrin family with higher neuronal uptake efficiency, which is inhibited by an integrin-blocking peptide (You *et al.*, 2020). Thus, EV uptake in Alzheimer's disease brains may be enhanced by differentially expressed EV surface proteins, due to altered cargo sorting or the origin of the cell type under neuroinflammatory conditions. It would be of interest to characterize molecules such as RNAs, HSPG, lipoproteins, and RNA-binding proteins, known to accelerate tau aggregation in Alzheimer's disease and pAD EVs for their contribution to tau propagation.

Extracellular vesicle-mediated GABAergic interneuronal dysfunction

We have also demonstrated EV-mediated propagation of tau in hippocampal GABAergic interneurons. Multiple lines of evidence have supported the notion that the dysfunction of GABAergic interneurons could be one of the critical components in the early pathogenesis of Alzheimer's disease. Decreased levels of GABA transmitter have been reported in the CSF of Alzheimer's disease patients and elderly individuals without cognitive impairment (Bareggi *et al.*, 1982; Zimmer *et al.*, 1984), as well as in the post-mortem tissues of Alzheimer's disease patients, especially in the temporal cortex, and to a lesser extent, the hippocampus, frontal cortex, and thalamus (Govindpani *et al.*, 2017). Alzheimer's disease patients showed loss of specific somatostatin$^+$ interneurons in the hippocampus and cortex (Davies *et al.*, 1980; Chan-Palay, 1987). Moreover, 7–21% of patients with sporadic Alzheimer's disease show at least one episode of seizure during the illness (Palop and Mucke, 2009), and administration of the anti-epileptic drug, levetiracetam, was effective for improving cognitive function in the elderly for those with normal memory, mild cognitive impairment, and Alzheimer's disease (Vossel *et al.*, 2013; Schoenberg *et al.*, 2017). In accordance with human study results, dysfunction of interneurons has been extensively reported in tauopathy animal models (Levenga *et al.*, 2013; Soler *et al.*, 2017). JNPL3 transgenic mice harbouring the *MAPT* P301L mutation show loss of hippocampal interneurons, PHF1$^+$ p-tau, and MC1$^+$ misfolded tau in interneurons, as well as a rescue of enhanced later phase long-term potentiation by administration of $GABA_A$ receptor agonist (Levenga *et al.*, 2013). VLW mice overexpressing human *MAPT* with three mutations (G272V, P301L, and R406W) show p-tau accumulation in hippocampal PV$^+$ GABAergic interneurons and mossy cells in dentate gyrus as early as 2 months of age (Soler *et al.*, 2017). Reduction of GABAergic septohippocampal innervation of PV$^+$ interneurons in VLW mice suggests tau accumulation may be responsible for GABAergic interneuronal loss (Soler *et al.*, 2017). We found that EV-mediated tau propagation in GABAergic interneurons causes neuronal dysfunction in the CA1 region, as determined by both immunohistochemistry and whole cell patch clamp recording. PV neurons are surrounded by the extracellular matrix structures called perineuronal nets, composed of integrin-binding versican and HSPGs (Deepa *et al.*, 2006). HSPGs have been shown to function as receptors for cancer cell-derived exosomes (Christianson *et al.*, 2013), implicating their specific role for EV uptake by GABAergic interneurons.

In summary, we have revealed a highly transmissible and potent seeding activity of Alzheimer's disease EVs with selective susceptibility of GABAergic interneurons and mossy cells in the hippocampal region. Our study creates a foundation to elucidate a novel EV-mediated tau spread mechanism, which may be relevant to interneuron dysfunction in Alzheimer's disease.

Acknowledgements

We would like to thank Drs Jean Christophe Delpech, and Annina DeLeo, and other members of the Laboratory of Molecular NeuroTherapeutics for scientific suggestions and technical assistance; Dr Peter Davies of Feinstein Institutes

for Medical Research for the generous gift of the Alz50, MC1, CP13, and PHF1 monoclonal antibodies, and Dr Benjamin Wolozin's laboratory members for technical assistance.

Funding

This work was funded in part by NIH R01 AG066429 (T.I.), RF1 AG054199 (T.I.), NIH R01 AG054672 (T.I.), NIH R56 AG057469 (T.I.), NIH R21 NS104609 (T.I.), NIH R01AG054025 (R.K.), NIH R01NS094557 (R.K.), Alzheimer's Association AARF-9550302678 (S.M.), Cure Alzheimer's Fund (T.I.), BrightFocus Foundation (A2016551S), CurePSP (T.I.) and BU ADC NIH P30 AG013846 (Z.R., S.I.).

Competing interests

The authors report no competing interests.

Supplementary material

Supplementary material is available at *Brain* online.

References

Apicco DJ, Ash PEA, Maziuk B, LeBlang C, Medalla M, Al Abdullatif A, et al. Reducing the RNA binding protein TIA1 protects against tau-mediated neurodegeneration in vivo. Nat Neurosci 2018; 21: 72–80.

Arai H, Clark CM, Ewbank DC, Takase S, Higuchi S, Miura M, et al. Cerebrospinal fluid tau protein as a potential diagnostic marker in Alzheimer's disease. Neurobiol Aging 1998; 19: 125–6.

Arriagada PV, Growdon JH, Hedley-Whyte ET, Hyman BT. Neurofibrillary tangles but not senile plaques parallel duration and severity of Alzheimer's disease. Neurology 1992; 42: 631–9.

Asai H, Ikezu S, Tsunoda S, Medalla M, Luebke J, Haydar T, et al. Depletion of microglia and inhibition of exosome synthesis halt tau propagation. Nat Neurosci 2015; 18: 1584–93.

Baker S, Polanco JC, Gotz J. Extracellular vesicles containing P301L mutant tau accelerate pathological tau phosphorylation and oligomer formation but do not seed mature neurofibrillary tangles in ALZ17 mice. J Alzheimers Dis 2016; 54: 1207–17.

Bareggi SR, Franceschi M, Bonini L, Zecca L, Smirne S. Decreased Csf concentrations of homovanillic-acid and gamma-aminobutyric acid in Alzheimers-disease—age-related or disease-related modifications. Arch Neurol 1982; 39: 709–12.

Barres C, Blanc L, Bette-Bobillo P, Andre S, Mamoun R, Gabius HJ, et al. Galectin-5 is bound onto the surface of rat reticulocyte exosomes and modulates vesicle uptake by macrophages. Blood 2010; 115: 696–705.

Bilousova T, Elias C, Miyoshi E, Alam MP, Zhu CN, Campagna J, et al. Suppression of tau propagation using an inhibitor that targets the DK-switch of nSMase2. Biochem Biophys Res Commun 2018; 499: 751–7.

Braak H, Braak E. Neuropathological stageing of Alzheimer-related changes. Acta Neuropathol 1991; 82: 239–59.

Brunello CA, Merezhko M, Uronen RL, Huttunen HJ. Mechanisms of secretion and spreading of pathological tau protein. Cell Mol Life Sci 2020; 77: 1721–44.

Budnik V, Ruiz-Canada C, Wendler F. Extracellular vesicles round off communication in the nervous system. Nat Rev Neurosci 2016; 17: 160–72.

Caraiscos VB, Elliott EM, You-Ten KE, Cheng VY, Belelli D, Newell JG, et al. Tonic inhibition in mouse hippocampal CA1 pyramidal neurons is mediated by alpha5 subunit-containing gamma-aminobutyric acid type A receptors. Proc Natl Acad Sci USA 2004; 101: 3662–7.

Chan-Palay V. Somatostatin immunoreactive neurons in the human hippocampus and cortex shown by immunogold/silver intensification on vibratome sections: coexistence with neuropeptide Y neurons, and effects in Alzheimer-type dementia. J Comp Neurol 1987; 260: 201–23.

Cheng L, Doecke JD, Sharples RA, Villemagne VL, Fowler CJ, Rembach A, et al. Prognostic serum miRNA biomarkers associated with Alzheimer's disease shows concordance with neuropsychological and neuroimaging assessment. Mol Psychiatry 2015; 20: 1188–96.

Christianson HC, Svensson KJ, van Kuppevelt TH, Li JP, Belting M. Cancer cell exosomes depend on cell-surface heparan sulfate proteoglycans for their internalization and functional activity. Proc Natl Acad Sci USA 2013; 110: 17380–5.

Colin M, Dujardin S, Schraen-Maschke S, Meno-Tetang G, Duyckaerts C, Courade JP, et al. From the prion-like propagation hypothesis to therapeutic strategies of anti-tau immunotherapy. Acta Neuropathol 2020; 139: 3–25.

Combs B, Tiernan CT, Hamel C, Kanaan NM. Production of recombinant tau oligomers in vitro. Methods Cell Biol 2017; 141: 45–64.

Cvjetkovic A, Jang SC, Konecna B, Hoog JL, Sihlbom C, Lasser C, et al. Detailed analysis of protein topology of extracellular vesicles-evidence of unconventional membrane protein orientation. Sci Rep 2016; 6: 36338.

Danzer KM, Kranich LR, Ruf WP, Cagsal-Getkin O, Winslow AR, Zhu LY, et al. Exosomal cell-to-cell transmission of alpha synuclein oligomers. Mol Neurodegener 2012; 7: 42.

Davies P, Katzman R, Terry RD. Reduced somatostatin-like immunoreactivity in cerebral cortex from cases of Alzheimer disease and Alzheimer senile dementa. Nature 1980; 288: 279–80.

Deepa SS, Carulli D, Galtrey C, Rhodes K, Fukuda J, Mikami T, et al. Composition of perineuronal net extracellular matrix in rat brain: a different disaccharide composition for the net-associated proteoglycans. J Biol Chem 2006; 281: 17789–800.

DeLeo AM, Ikezu T. Extracellular vesicle biology in Alzheimer's disease and related tauopathy. J Neuroimmune Pharmacol 2018; 13: 292–308.

Delpech JC, Herron S, Botros MB, Ikezu T. Neuroimmune crosstalk through extracellular vesicles in health and disease. Trends Neurosci 2019; 42: 361–72.

Dujardin S, Begard S, Caillierez R, Lachaud C, Delattre L, Carrier S, et al. Ectosomes: a new mechanism for non-exosomal secretion of tau protein. PLoS One 2014; 9: e100760.

Evans LD, Wassmer T, Fraser G, Smith J, Perkinton M, Billinton A, et al. Extracellular monomeric and aggregated tau efficiently enter human neurons through overlapping but distinct pathways. Cell Rep 2018; 22: 3612–24.

Falcon B, Zhang WJ, Murzin AG, Murshudov G, Garringer HJ, Vidal R, et al. Structures of filaments from Pick's disease reveal a novel tau protein fold. Nature 2018; 561: 137–40.

Falcon B, Zivanov J, Zhang WJ, Murzin AG, Garringer HJ, Vidal R, et al. Novel tau filament fold in chronic traumatic encephalopathy encloses hydrophobic molecules. Nature 2019; 568: 420–3.

Fevrier B, Vilette D, Archer F, Loew D, Faigle W, Vidal M, et al. Cells release prions in association with exosomes. Proc Natl Acad Sci USA 2004; 101: 9683–8.

Fiandaca MS, Kapogiannis D, Mapstone M, Boxer A, Eitan E, Schwartz JB, et al. Identification of preclinical Alzheimer's disease by a profile of pathogenic proteins in neurally derived blood exosomes: a case-control study. Alzheimers Dementia 2015; 11: 600–7.

Fitzpatrick AWP, Falcon B, He S, Murzin AG, Murshudov G, Garringer HJ, et al. Cryo-EM structures of tau filaments from Alzheimer's disease. Nature 2017; 547: 185–90.

Ghag G, Bhatt N, Cantu DV, Guerrero-Munoz MJ, Ellsworth A, Sengupta U, et al. Soluble tau aggregates, not large fibrils, are the toxic species that display seeding and cross-seeding behavior. Protein Sci 2018; 27: 1901–9.

Govindpani K, Guzman BCF, Vinnakota C, Waldvogel HJ, Faull RL, Kwakowsky A. Towards a better understanding of GABAergic remodeling in Alzheimer's disease. Int J Mol Sci 2017; 18: 1813.

Grad LI, Fernando SM, Cashman NR. From molecule to molecule and cell to cell: prion-like mechanisms in amyotrophic lateral sclerosis. Neurobiol Dis 2015; 77: 257–65.

Guo JL, Narasimhan S, Changolkar L, He Z, Stieber A, Zhang B, et al. Unique pathological tau conformers from Alzheimer's brains transmit tau pathology in nontransgenic mice. J Exp Med 2016; 213: 2635–54.

Hatch RJ, Wei Y, Xia D, Gotz J. Hyperphosphorylated tau causes reduced hippocampal CA1 excitability by relocating the axon initial segment. Acta Neuropathol 2017; 133: 717–30.

He B, Liu L, Cook GA, Grgurevich S, Jennings LK, Zhang XA. Tetraspanin CD82 attenuates cellular morphogenesis through down-regulating integrin alpha 6-mediated cell adhesion. J Biol Chem 2005; 280: 3346–54.

Holmes BB, Furman JL, Mahan TE, Yamasaki TR, Mirbaha H, Eades WC, et al. Proteopathic tau seeding predicts tauopathy in vivo. Proc Natl Acad Sci USA 2014; 111: E4376–85.

Hoshino A, Costa-Silva B, Shen TL, Rodrigues G, Hashimoto A, Mark MT, et al. Tumour exosome integrins determine organotropic metastasis. Nature 2015; 527: 329–35.

Hu W, Zhang XH, Tung YC, Xie ST, Liu F, Iqbal K. Hyperphosphorylation determines both the spread and the morphology of tau pathology. Alzheimers Dement 2016; 12: 1066–77.

Im H, Shao HL, Park YI, Peterson VM, Castro CM, Weissleder R, et al. Label-free detection and molecular profiling of exosomes with a nano-plasmonic sensor. Nat Biotechnol 2014; 32: 490–5.

Jiang LL, Ash PEA, Maziuk BF, Ballance HI, Boudeau S, Al Abdullatif A, et al. TIA1 regulates the generation and response to toxic tau oligomers. Acta Neuropathol 2019; 137: 259–77.

Keren-Shaul H, Spinrad A, Weiner A, Matcovitch-Natan O, Dvir-Szternfeld R, Ulland TK, et al. A unique microglia type associated with restricting development of Alzheimer's disease. Cell 2017; 169: 1276–90.

Kinney JW, Bemiller SM, Murtishaw AS, Leisgang AM, Salazar AM, Lamb BT. Inflammation as a central mechanism in Alzheimer's disease. Alzheimers Dement (N Y) 2018; 4: 575–90.

Krasemann S, Madore C, Cialic R, Baufeld C, Calcagno N, El Fatimy R, et al. The TREM2-APOE pathway drives the transcriptional phenotype of dysfunctional microglia in neurodegenerative diseases. Immunity 2017; 47: 566–81.

Lambert JC, Heath S, Even G, Campion D, Sleegers K, Hiltunen M, et al. Genome-wide association study identifies variants at CLU and CR1 associated with Alzheimer's disease. Nat Genet 2009; 41: 1094–9.

Levenga J, Krishnamurthy P, Rajamohamedsait H, Wong H, Franke TF, Cain P, et al. Tau pathology induces loss of GABAergic interneurons leading to altered synaptic plasticity and behavioral impairments. Acta Neuropathol Commun 2013; 1: 34.

Mathys H, Davila-Velderrain J, Peng ZY, Gao F, Mohammadi S, Young JZ, et al. Single-cell transcriptomic analysis of Alzheimer's disease. Nature 2019; 570: 332–7.

McAvoy KM, Soit HR, Marsh G, Peterson M, Reynolds TL, Gagnon J, et al. Cell-autonomous and non-cell autonomous effects of neuronal BIN1 loss in vivo. PLoS One 2019; 14: e0220125.

Mirbaha H, Holmes BB, Sanders DW, Bieschke J, Diamond MI. Tau trimers are the minimal propagation unit spontaneously internalized to seed intracellular aggregation. J Biol Chem 2015; 290: 14893–903.

Morelli AE, Larregina AT, Shufesky WJ, Sullivan MLG, Stolz DB, Papworth GD, et al. Endocytosis, intracellular sorting, and processing of exosomes by dendritic cells. Blood 2004; 104: 3257–66.

Mulcahy LA, Pink RC, Carter DR. Routes and mechanisms of extracellular vesicle uptake. J Extracell Vesicles 2014; 3: 24641.

Muraoka S, DeLeo AM, Sethi MK, Yukawa-Takamatsu K, Yang Z, Ko J, et al. Proteomic and biological profiling of extracellular vesicles from Alzheimer's disease human brain tissues. Alzheimers Dement 2020a; 16: 896–907.

Muraoka S, Jedrychowski MP, Tatebe H, DeLeo AM, Ikezu S, Tokuda T, et al. Proteomic profiling of extracellular vesicles isolated from cerebrospinal fluid of former national football league players at risk for chronic traumatic encephalopathy. Front Neurosci 2019; 13: 1059.

Muraoka S, Lin W, Chen M, Hersh SW, Emili A, Xia W, et al. Assessment of separation methods for extracellular vesicles from human and mouse brain tissues and human cerebrospinal fluids. Methods 2020b; 177: 35–49.

Narasimhan S, Guo JL, Changolkar L, Stieber A, McBride JD, Silva LV, et al. Pathological tau strains from human brains recapitulate the diversity of tauopathies in nontransgenic mouse brain. J Neurosci 2017; 37: 11406–23.

Nazarenko I. Cell surface tetraspanin tspan8 contributes to molecular pathways of exosome-induced endothelial cell activation. Cancer Res 2010; 70: 1668–78.

Palop JJ, Mucke L. Epilepsy and cognitive impairments in Alzheimer disease. Arch Neurol 2009; 66: 435–40.

Perez-Gonzalez R, Gauthier SA, Kumar A, Levy E. The exosome secretory pathway transports amyloid precursor protein carboxyl-terminal fragments from the cell into the brain extracellular space. J Biol Chem 2012; 287: 43108–15.

Polanco JC, Scicluna BJ, Hill AF, Gotz J. Extracellular vesicles isolated from the brains of rTg4510 mice seed tau protein aggregation in a threshold-dependent manner. J Biol Chem 2016; 291: 12445–66.

Purushothaman A, Bandari SK, Liu J, Mobley JA, Brown EE, Sanderson RD. Fibronectin on the surface of myeloma cell-derived exosomes mediates exosome-cell interactions. J Biol Chem 2016; 291: 1652–63.

Quast T, Eppler F, Semmling V, Schild C, Homsi Y, Levy S, et al. CD81 is essential for the formation of membrane protrusions and regulates Rac1-activation in adhesion-dependent immune cell migration. Blood 2011; 118: 1818–27.

Ruan Z, Ikezu T. Tau secretion. Adv Exp Med Biol 2019; 1184: 123–34.

Saman S, Kim W, Raya M, Visnick Y, Miro S, Saman S, et al. Exosome-associated tau is secreted in tauopathy models and is selectively phosphorylated in cerebrospinal fluid in early Alzheimer disease. J Biol Chem 2012; 287: 3842–9.

Schoenberg MR, Rum RS, Osborn KE, Werz MA. A randomized, double-blind, placebo-controlled crossover study of the effects of levetiracetam on cognition, mood, and balance in healthy older adults. Epilepsia 2017; 58: 1566–74.

Sengupta U, Carretero-Murillo M, Kayed R. Preparation and characterization of tau oligomer strains. Methods Mol Biol 2018; 1779: 113–46.

Sigurdsson EM. Tau immunotherapies for Alzheimer's disease and related tauopathies: progress and potential pitfalls. J Alzheimers Dis 2018; 66: 855–6.

Soler H, Dorca-Arevalo J, Gonzalez M, Rubio SE, Avila J, Soriano E, et al. The GABAergic septohippocampal connection is impaired in a mouse model of tauopathy. Neurobiol Aging 2017; 49: 40–51.

Stern RA, Tripodis Y, Baugh CM, Fritts NG, Martin BM, Chaisson C, et al. Preliminary study of plasma exosomal tau as a potential

biomarker for chronic traumatic encephalopathy. J Alzheimers Dis 2016; 51: 1099–109.

Sung BH, Ketova T, Hoshino D, Zijlstra A, Weaver AM. Directional cell movement through tissues is controlled by exosome secretion. Nat Commun 2015; 6: 7164.

van Niel G, D'Angelo G, Raposo G. Shedding light on the cell biology of extracellular vesicles. Nat Rev Mol Cell Biol 2018; 19: 213–28.

Volz F, Bock HH, Gierthmuehlen M, Zentner J, Haas CA, Freiman TM. Stereologic estimation of hippocampal GluR2/3-and calretinin-immunoreactive hilar neurons (presumptive mossy cells) in two mouse models of temporal lobe epilepsy. Epilepsia 2011; 52: 1579–89.

Vossel KA, Beagle AJ, Rabinovici GD, Shu HD, Lee SE, Naasan G, et al. Seizures and epileptiform activity in the early stages of Alzheimer disease. Jama Neurol 2013; 70: 1158–66.

Winston CN, Aulston B, Rockenstein EM, Adame A, Prikhodko O, Dave KN, et al. Neuronal exosome-derived human tau is toxic to recipient mouse neurons in vivo. J Alzheimers Dis 2019; 67: 541–53.

Winston CN, Goetzl EJ, Akers JC, Carter BS, Rockenstein EM, Galasko D, et al. Prediction of conversion from mild cognitive impairment to dementia with neuronally derived blood exosome protein profile. Alzheimers Dement (Amst) 2016; 3: 63–72.

Yamada K, Holth JK, Liao F, Stewart FR, Mahan TE, Jiang H, et al. Neuronal activity regulates extracellular tau in vivo. J Exp Med 2014; 211: 387–93.

You Y, Borgmann K, Edara VV, Stacy S, Ghorpade A, Ikezu T. Activated human astrocyte-derived extracellular vesicles modulate neuronal uptake, differentiation and firing. J Extracell Vesicles 2020; 9: 1706801.

You Y, Ikezu T. Emerging roles of extracellular vesicles in neurodegenerative disorders. Neurobiol Dis 2019; 130: 104512.

Zetterberg H, Wilson D, Andreasson U, Minthon L, Blennow K, Randall J, et al. Plasma tau levels in Alzheimer's disease. Alzheimers Res Ther 2013; 5: 9.

Zhang WJ, Tarutani A, Newell KL, Murzin AG, Matsubara T, Falcon B, et al. Novel tau filament fold in corticobasal degeneration. Nature 2020; 580: 283–287.

Zimmer R, Teelken AW, Trieling WB, Weber W, Weihmayr T, Lauter H. Gamma-aminobutyric acid and homovanillic-acid concentration in the Csf of patients with senile dementia of Alzheimers type. Arch Neurol 1984; 41: 602–4.